STUDYING MOUSE EMBRYONIC DEVELOPMENT WITH OCT

A Dissertation

Presented to

the Faculty of the Department of Biomedical Engineering

University of Houston

In Partial Fulfillment

of the Requirements for the Degree of

Doctor of Philosophy

in Biomedical Engineering

by

Narendran Sudheendran

December 2013

STUDYING MOUSE EMBRYONIC DEVELOPMENT WITH OCT

_____

Narendran Sudheendran

Approved:

_____

Chair of the Committee
Kirill V. Larin, Associate Professor,
Department of Biomedical Engineering

Committee Members:

_____

Irina V. Larina, Assistant Professor,
Department of Molecular Physiology and Biophysics, Baylor College of Medicine

_____

Rajesh C. Miranda, Associate Professor,
Department of Neuroscience and Experimental Therapeutics, TAMHSC College of Medicine

_____

Howard Gifford, Associate Professor,
Department of Biomedical Engineering

_____

Yingchun Zhang, Assistant Professor,
Department of Biomedical Engineering

_____

Suresh K. Khator, Associate Dean,
Cullen College of Engineering

_____

Metin Akay, Professor and Chairman,
Department of Biomedical Engineering

ACKNOWLEDGEMENTS

I am extremely thankful to my advisor, Dr. Kirill Larin, for his guidance, support and encouragement throughout this work. I am extremely grateful to Dr. Irina Larina for her time and effort to help me during the entire course of my project. I would especially like to thank Saba, Maleeha, Dr. Shameena Bake and Chen for helping me with the experiments. I thank Esteban, Shang and Manmohan for reviewing my dissertation. I am thankful to Mohamad, Kiran, Venu, Stepan, Jiasong, Peter and the rest of the BOL team for their support and encouragement.

I would like to thank Dr. Rajesh C. Miranda and Dr. Howard Gifford and Dr. Yingchun Zhang for their time to serve on my defense committee.

I dedicate this dissertation to my parents, Sachin, Shruti, Vedant, Arin and my friends.

STUDYING MOUSE EMBRYONIC DEVELOPMENT WITH OCT

An Abstract

of a

Dissertation

Presented to

the Faculty of the Department of Biomedical Engineering

University of Houston

In Partial Fulfillment

of the Requirements for the Degree

Doctor of Philosophy

in Biomedical Engineering

by

Narendran Sudheendran

December 2013

ABSTRACT

Live imaging of mammalian embryos can elucidate human embryonic development, which is governed by several genetic and environmental factors. Improvements in the acquisition and quality of imaging modalities can potentially contribute to understanding, prevention, and, eventually, treatment of congenital birth defects. This dissertation is devoted to investigate the morphological changes which are associated with mouse embryonic development, using optical coherence tomography (OCT). Firstly, the remodeling of the yolk sac vasculature in a mouse embryo is analyzed. Detection of 3D vasculature using Doppler OCT and speckle variance (SV) OCT were compared. The results demonstrate that SVOCT provides more accurate representation of the vascular structure, as it is not sensitive to the blood flow direction. Secondly, the development of ocular tissues from E13.5 to E18.5 was monitored *in utero*. The volumes of the eye lens and eye globe was used as the parameter to monitor the development of ocular structures. Results demonstrated the capability of OCT for high-resolution, high-contrast imaging of ocular development in mouse embryos *in utero*. Thirdly, OCT was compared with high-resolution ultrasound (US) to study the effects of prenatal exposure to ethanol on brain development. Volume of the lateral ventricles was used to assess the effect of ethanol exposure between the control and ethanol-exposed fetuses. The results demonstrated that the volume of lateral ventricles was twice as high in ethanol-exposed fetuses compared to the control ones. The results also demonstrated clear advantages of using OCT for quantitative assessment of embryonic brain development compared to US imaging.

TABLE OF CONTENTS

LIST OF FIGURES

Chapter 1. Optical Coherence Tomography

1.1 Introduction

Optical coherence tomography (OCT) is an optical imaging modality capable of depth resolved noninvasive 2D and 3D structural and functional imaging of biological tissues [1-4]. OCT is analogous to ultrasound imaging as it obtains in-depth information by measuring echo-time delay of photons scattered (back-reflected) from different layers (optical boundaries or refractive index discontinuities) of a sample instead of ultrasonic pulses. Due to the fact that light travels much faster than sound, present day detectors cannot resolve the time delays of a photons coming from micron-thick layers of a sample. This prompts the use of indirect methods to resolve these extremely small time delays. For this purpose, OCT employs the principle of light interference by using an interferometer. Contrast in OCT structural and functional images arises due to optical interaction of light with tissue (absorption and scattering); therefore it requires no external contrast agents. OCT typically provides an axial resolution of ~2-20 μm and an imaging depth of a few mm. Since its introduction in 1991 [1], OCT has been extensively applied in various biomedical fields. OCT has shown its potential in the field of ophthalmology [1], dermatology [5], dentistry [6], gastroenterology [7], tissue engineering [8], amongst others. Besides providing structural information, OCT has also been implemented to perform functional information such as flow dynamics within a biological tissue [9, 10]. Over the last few years, OCT has successfully bridged the gap between the macro-scale imaging modalities such as MRI and ultrasonography and micro-scale modalities such as confocal microscopy.

1.2 Theory

1.2.1 Low coherence interferometry

Low coherence interferometry (LCI) is a nonscanning version of OCT and typically employs a Michelson interferometer, with a broadband laser in the source arm, a beam-splitter, and a photodetector in the detector arm (Figure 1.1). The beam-splitter splits the light (usually 50:50) into a reference and a sample arm. The back-reflected light from the reference and sample arms interfere at the beam-splitter and the resulting interference pattern is detected by the photodetector. The broadband laser source in the source arm has low time coherence, hence, interference between a particular layer of a sample and the reference arm mirror is detected only when their optical path difference is within the coherence length of the laser. A complete depth scan (A-scan) is obtained by axially scanning the reference arm mirror as represented in Figure 1.1.

A biological sample can be modeled as an ensemble of discrete reflectors/scatterers. Mathematically they can be represented as,

$$r_s(z_s) = \sum_{n=1}^{N} r_{sn}\delta(z_s - z_{sn}), \tag{1.1}$$

where, r_{sn} is the reflectivity of the nth reflector at a path difference of z_{sn} from the reference arm mirror [11]. The current at the photodetector I_D, as the reference arm axially scans across z_R, is given by,

$$I_D(z_R) \propto \frac{\rho}{2}\left[S_0 \sum_{n=1}^{N}\left(\sqrt{R_R R_{Sn}}\, e^{-(z_R - z_{sn})^2 \Delta k^2} \cos[2k_0(z_R - z_{sn})]\right) \right], \tag{1.2}$$

where, ρ is the responsivity of detector, S_0 is the integrated spectrum power, R_R is the reflectivity of the mirror at reference arm, R_{Sn} is the reflectivity of the nth sample reflector, z_R is the path length of the mirror at the reference arm from the beam-splitter, z_{sn} is the path length of the nth sample reflector from the beam-splitter, k_0 and Δk are the central wavenumber and bandwidth wavenumber of laser source. The plot of the current detected at the photodetector with the axial scanning length of the mirror at the reference arm is referred to as an A-scan.

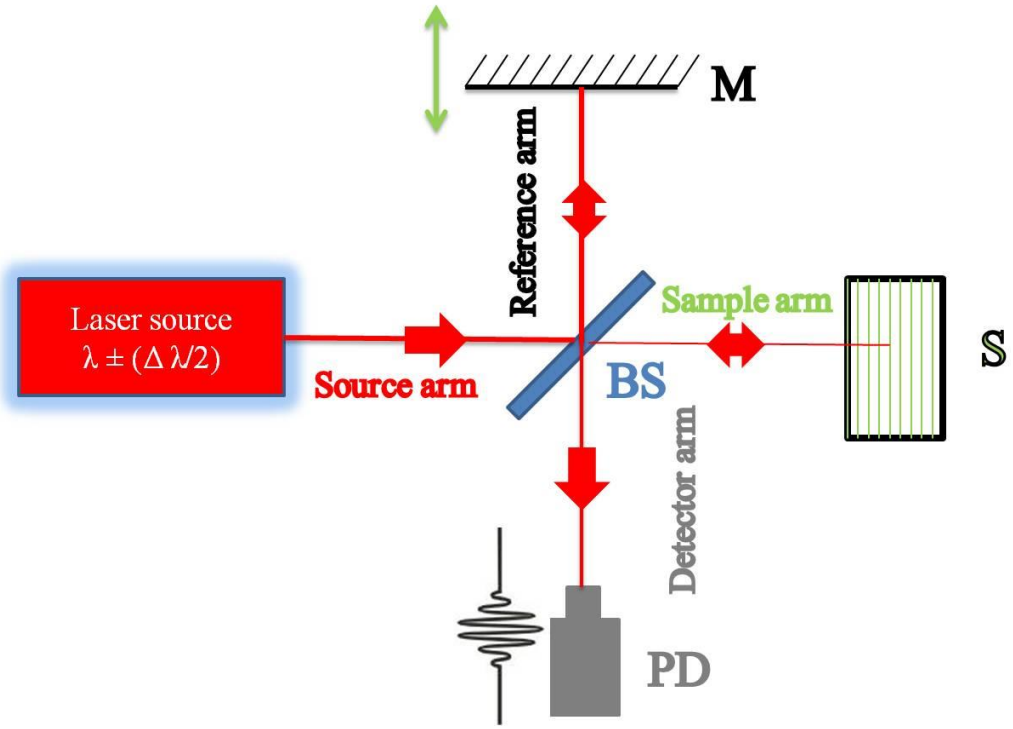

Figure 1.1. General schematic of a LCI system. λ - central wavelength of the laser source, Δλ - bandwidth of the laser source, M - Mirror, S - Sample, BS- Beamsplitter and PD – Photodetector.

1.2.2 Time-Domain OCT

Time-Domain OCT (TDOCT) is an extension of LCI, first introduced in 1991 in the field of ophthalmology [1]. TDOCT employs a moving mirror in the reference arm to perform in-depth scanning of the sample. Galvanometer mounted mirrors (galvos) perform transverse scanning across tissue surface to form 2D (B-scans) and 3D images

(C-scans). Scanning of the mirror in the reference arm can also be performed using a rapid scanning optical delay line (RSOD) instead of mechanical movement of the mirror along z-direction [12]. Nevertheless, requirement of mechanical movement of the mirror in the reference arm limits the speed of image acquisition in TDOCT systems (up to a few kHz). However, it is preferred for ophthalmological applications due to its ability to provide high imaging depths (limited basically by how much the reference mirror can be translocated).

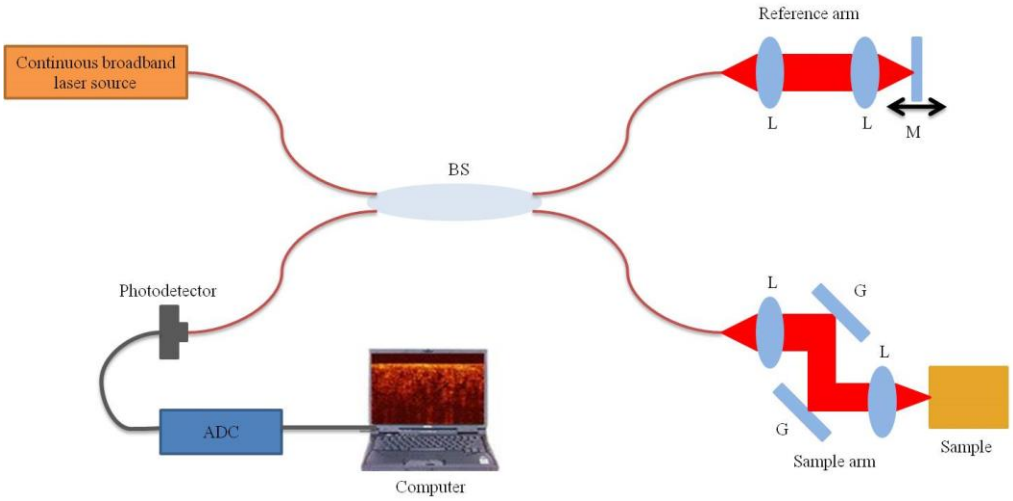

Figure 1.2. General schematic diagram of a TDOCT system. BS – Beamsplitter. L – Lens. M – Mirror. G – Galvanometer mounted mirrors.

1.2.3 Fourier-Domain OCT

Alternative to the time-domain approach, the depth information can be obtained by spatially resolving the laser spectrum into its frequency components. Due to Fourier relation (Weiner-Khintchin theorem) between the autocorrelation and the spectral power density, the depth information of the sample is encoded as a function of frequency of the laser spectrum which is linear in wavenumber space (k-space). The mathematical representation of the detected current for a multi-layered sample is given by

$$I_D(z) \propto \frac{\rho}{4}[\,\gamma(z) * \sum_{n=1}^{N}(\sqrt{R_R R_{Sn}}\,\delta[z + 2(z_R - z_{sn})])], \quad (1.3)$$

where, $\gamma(z)$ is the inverse Fourier transform of the laser source spectrum S(k). Fourier-Domain OCT (FDOCT) is further classified into two subtypes based on their method to resolve the wavenumbers of the laser spectrum: Spectral-Domain OCT and Swept-source OCT.

1.2.3.1 Spectral-Domain OCT

Spectral-Domain OCT (SDOCT) resolves the wavenumbers using a spectrometer instead of a photodetector at the detector arm (Figure 1.3). The spectrometer typically comprises of a diffraction grating, a focusing lens and a CCD/CMOS array [13]. The diffraction grating spatially separates the source spectrum as a linear function of wavelengths instead of linear in k-space. This mandates the use of calibration techniques for linear k-space conversion before application of Fourier transformation. Recently, modifications have been made in the spectrometer by incorporating a prism, which spatially separates the spectrum linear in wavenumber [14]. This saves computational time as linear k-space interpolation techniques are no longer required.

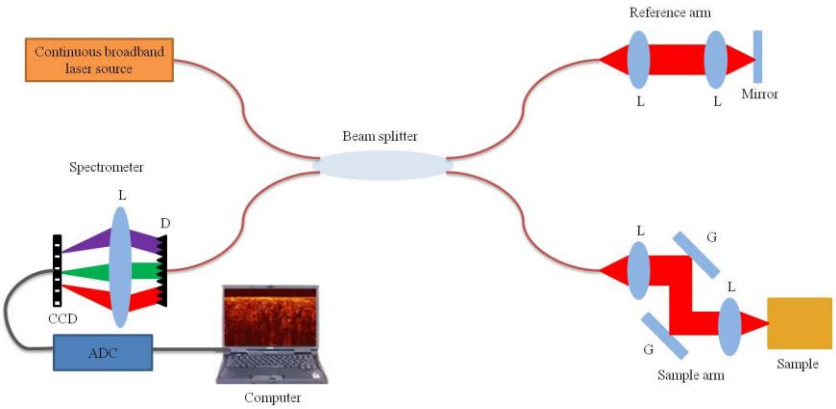

Figure 1.3. General schematic of a SDOCT system. BS – Beamsplitter. L – Lens. M – Mirror. G – Galvanometer mounted mirrors

1.2.3.2 Swept-source OCT (SSOCT)

An alternative approach to SDOCT is to resolve the wavenumbers at the source rather than at the detector end. A sweeping wavelengths laser source is the center of a swept-source OCT (SSOCT) system [15]. Instead of a spectrometer, the SSOCT system employs a photodetector (Figure 1.4). The spectrum swept by the laser source linear in wavelength. An external interferometer, such as Mach-Zehnder interferometer (MZI) or Fabry-Perot interferometer (FP) are often employed for conversion into linear k-space [16, 17]. The peaks, troughs and the zero crossings from the interferometric signal detected using MZI or FP correspond to indices which are linear in k-space. Hence, the corresponding indices from the raw signal, detected by the photodetector, are chosen to reconstruct the depth information. Recent developments have been made in Fourier-domain mode locking (FDML) laser technology which can produce linear wavenumbers in time, thus saving time that would be needed for linear k-space conversion [18].

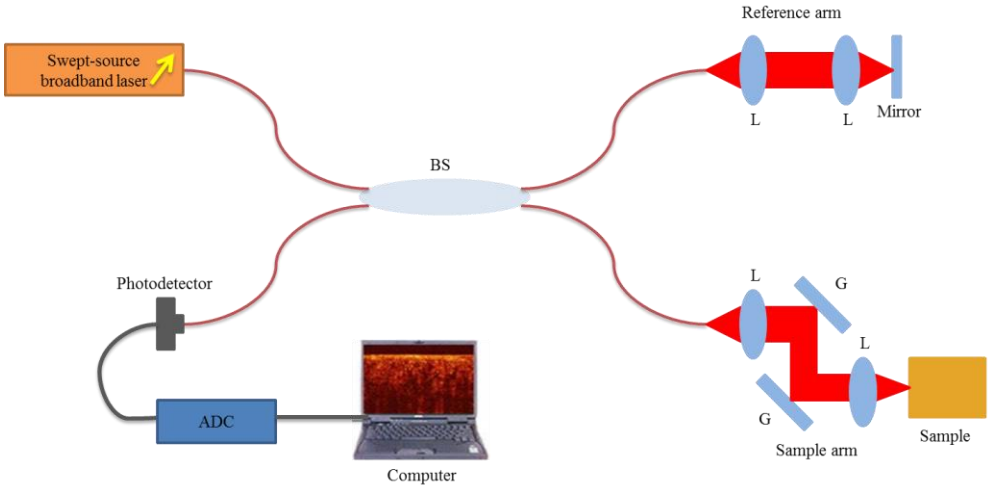

Figure 1.4. General schematic of a SSOCT system. BS – Beamsplitter. L – Lens. M – Mirror. G – Galvanometer mounted mirrors

1.2.4 OCT system parameters

Axial resolution, transverse resolution, imaging depth, imaging acquisition speed and signal-to-noise ratio (SNR) are a few parameters which are often used to evaluate OCT systems. These parameters have been described in this section.

1.2.4.1 Axial resolution

The use of low coherence light in OCT enables it to resolve depth information as interference is recorded only when the optical path difference between the reference and the sample arms matches within the coherence length of the laser source. The axial resolution Δz, is numerically evaluated as,

$$\Delta z = \frac{2 \ln 2}{\pi} \frac{{\lambda_0}^2}{\Delta\lambda}, \tag{1.4}$$

where, $\frac{{\lambda_0}^2}{\Delta\lambda}$ is the coherence length of the laser source. A broadband source with low central wavelength (λ_0) and high bandwidth ($\Delta\lambda$) has a low coherence length, as indicated by equation 1.4. For example, for the same bandwidth a source with a central wavelength of 860 nm has a better resolution than compared to a source with a central wavelength of 1300 nm (Figure 1.5). The axial resolution is completely determined by the laser source characteristics unlike other optical imaging modalities, where axial resolution depends on the characteristics of the optics used in the system. The axial resolution of an OCT system is often degraded by dispersion mismatch between the reference and the sample arms. Dispersion compensation optics are often employed to resolve this issue [19].

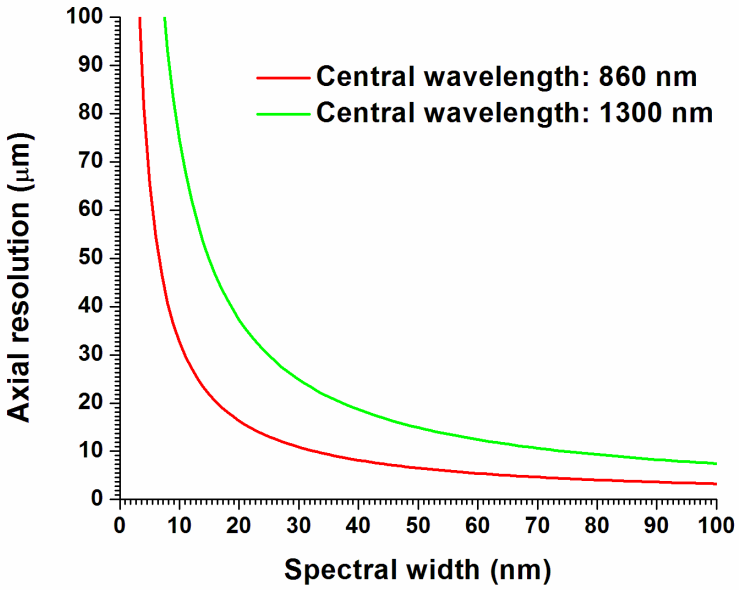

Figure 1.5. Plot of axial resolution versus spectral width (Δλ) for central wavelengths (λ0) of 860 and 1300 nm.

1.2.4.2 Transverse resolution

The transverse resolution in OCT is determined by the focusing optics used in the sample arm. Numerically, transverse resolution (Δx) is evaluated as,

$$\Delta x = \frac{2\lambda_0}{\pi}\frac{1}{NA}, \tag{1.5}$$

where, NA is the numerical aperture of the focusing lens used in the sample arm. A high NA results in a better transverse resolution, however, it reduces the depth of focus of the laser beam.

1.2.4.3 Imaging depth

In a TDOCT system, the imaging depth is determined by the extent to which the mirror at the reference arm can be translated. Theoretically, the imaging depth can extend

to infinity in a clear medium, considering that the mirror at reference arm can be translated to infinity.

In a FDOCT system, the imaging depth is determined by the spectral resolution of the system. The spectral resolution is determined by the characteristics of the spectrometer in a SDOCT system, and the spatial pulse width of the swept-source laser in a SSOCT system. Theoretical imaging depth can be evaluated from,

$$z_{max} = \frac{{\lambda_0}^2}{4\delta\lambda}, \tag{1.6}$$

where, $\delta\lambda$ is the spectral resolution. The spectral resolution determines the Nyquist criterion which limits the imaging depth.

1.2.4.4 Image acquisition speed

The speed of a TDOCT system is limited by the mechanical movement of the mirror in the reference arm. The time for A-scan acquisition is determined by the time taken by the reference arm to complete a single scan.

FDOCT systems are much faster than TDOCT systems as there is no mechanical movement of the reference mirror is required. The entire A-scan is captured as a single shot of the CCD/CMOS line camera in a SDOCT system. A-scan rates up to 312 kHz have been recorded using a SDOCT system [20]. In a SSOCT system, the A-scan rate is determined by the sweeping rate of the swept-source laser. Speeds up to 20 MHz have been shown using buffered Fourier domain mode locked lasers (FDML) [21].

1.2.4.5 Signal-to-noise ratio

The signal-to-noise ratio (SNR) for a TDOCT system is given by,

$$SNR_{TDOCT} = \frac{\rho S_{TDOCT} R_S}{2eB_{TDOCT}}, \quad (1.7)$$

where, ρ is the responsivity of the detector, S_{TDOCT} is the instantaneous source power, R_S is the reflectivity of the sample, e is the electronic charge and $B_{TDOCT}$is the electronic detection bandwidth [11].

The SNR for a FDOCT system is given by,

$$SNR_{FDOCT} = \frac{\rho S_{FDOCT}[k_m] R_S}{4eB_{FDOCT}} M, \quad (1.8)$$

where, $S_{FDOCT}[k_m]$ is the instantaneous power at wavenumber k_m, M number of sampling points, B_{FDOCT} is the electronic detection bandwidth [11].

Previous studies have proved the sensitivity advantages of FDOCT over TDOCT up to 30 dB [22-24]. Due to the finite resolution of wavelengths in FDOCT systems, they suffer from sensitivity drop off as imaging depth increases. This effect is more pronounced in SDOCT as compared to SSOCT, where the effect is less pronounced [25].

1.2.5 Speckle in OCT

Speckle is a natural consequence in OCT due to use of coherent light source. Biological tissues are optically inhomogeneous media and cause multiple scattering of the incident light which distorts its phase as is propagates within the tissue. Speckle arises as a consequence of interference of the multiply scattered beam with random phase [26]. Being a random phenomenon, speckle distribution is described by it statistical properties.

The probability of measuring intensity (I), in a fully developed speckle is given by a negative-exponential density function as,

$$p(I) = \frac{1}{<I>} e^{-\frac{I}{<I>}}. \quad (1.9)$$

Speckle in OCT is considered as a source of noise for most applications as it degrades the contrast of the image and makes it difficult to resolve boundaries between different layers in the tissue. Numerous methods have been devised to reduce speckle noise in OCT images [27-31]. However, the speckle is also a carrier of information about the underlying tissue and can be used to, e.g., distinguish between different tissue types [32, 33].

1.3 Flow detection using OCT

1.3.1 Doppler OCT

Doppler OCT (DOCT) uses the Doppler shift information which is caused by axial movement of the dynamic scatterers. Simple DOCT images can be obtained by subtracting phase from consecutive A-scans using the Kasai autocorrelation function [34],

$$\Delta\phi = tan^{-1}\left[\frac{\sum_{m=1}^{M}\sum_{n=1}^{N}\left(I_{m,n+1}Q_{m,n} - Q_{m,n+1}I_{m,n}\right)}{\sum_{m=1}^{M}\sum_{n=1}^{N}\left(Q_{m,n+1}Q_{m,n} + I_{m,n+1}I_{m,n}\right)}\right], \quad (1.10)$$

where, $\Delta\phi$ is the change in phase between consecutive A-scans, M is the vertical window size, N is the horizontal window size, and I and Q are the real and complex part of the signal obtained after performing fast Fourier transform (FFT) on the calibrated signal [35].

The change in phase is directly proportional to the axial velocity component as

$$\Delta\phi = v(2n\frac{2\pi}{\lambda_0}\tau\cos(\beta)), \tag{1.11}$$

where, v is the velocity of the dynamic scatterer, n is the refractive index of the meduim, λ_0 is the central wavelength of the laser source, τ is the acquisition time between consecutive A-scans and β is the angle made by the velocity vector of the dynamic scatterer with respect to the laser beam [36]. For a static scatterer, the ideal phase difference is zero. It is clear from equation 1.11 that in order to calculate velocity of blood flow it is necessary to determine the angle, β. DOCT heavily relies on the phase stability of the system and extremely sensitive to external disturbances. It is also observed from equation 1.11 that phase difference is zero when $\beta = 90°$. This implies that if the blood vessel is perpendicular to the laser beam, DOCT will not be able to distinguish moving components from static tissues. These are the major disadvantages of DOCT for detection of 3D vasculature.

1.3.2 Optical micro-angiography

Recently, optical micro-angiography (OMAG) was developed by Dr. R. Wang using the same principle as obtaining full length imaging by introducing a modulation frequency by reference arm translation [37]. Considering the reference arm velocity to be v_{ref} and the velocity of transverse scanning to be v_x, the spectral interferogram in λ domain can be represented as,

$$B\left(\frac{1}{\lambda}, x\right) = \cos(\frac{4\pi\left(z_s + (v_{ref}+v_s)\frac{x}{v_x}\right)}{\lambda} + \Phi(x,z,\lambda)), \tag{1.12}$$

where, x and z_s are the transverse and axial position of the scatterer respectively, v_s is the velocity of the scatterer and $\Phi(x,z,\lambda)$ is the phase [37]. Unlike conventional OCT,

Hilbert transform is performed along the x direction prior to applying Fourier transform. Only if $|v_s| > |v_{ref}|$ such that v_s and v_{ref} are in opposite directions, the scatterer will appear in the negative side of Fourier transform. In all other cases, the scatterer will appear in the positive side of the Fourier transform. Hence, OMAG effectively differentiates dynamic scatterers from static scatterers. Modulation frequency can also be introduced using offsetting of galvos. Further modifications have been introduced since OMAG was first introduced, allowing it to be used to image bidirectional flow and quantify flow using Doppler information, especially to detect cerebral blood flow [38-40]. Even though OMAG has been used for 3D vasculature detection (an example is shown in Figure 1.6), its insensitivity to transverse flow is still a limitation.

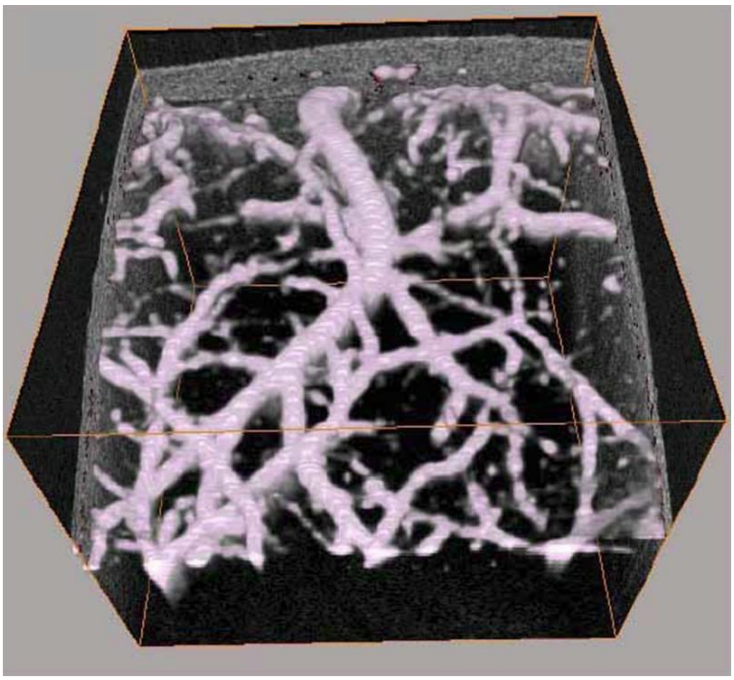

Figure 1.6. Typical image of an adult mouse brain obtained using OMAG. Adapted from [37].

1.3.3 Phase contrast

Phase contrast method was implemented to generate 3D image vasculature in a zebra fish [41]. This method estimates the variance of phase in dynamic and static

scatterers to detect flow. This method has been successful in detection of both axial and transverse components of flow; however, it is extremely sensitive to phase stability of the system and external disturbances.

1.3.4 Speckle variance imaging

Similar to phase contrast imaging, variance of time-varying speckle can be used to detect both axial and transverse flow components. The speckles in OCT images caused by dynamic scatterers decorrelate much faster than speckles from static scatteres in a biological tissue. Hence, by determining the pixel variance in from OCT structural image over time, blood vessels can be detected. Speckle variance (SV) images can be constructed by implementing a simple variance algorithm,

$$SV_{i,j} = \frac{1}{N} \sum_{t=0}^{N-1} (I_{i,j,t} - I_{i,j,mean})^2 \,, \tag{1.13}$$

where, $SV_{i,j}$ is the variance at the pixel(i,j), $I_{i,j,t}$ is the structural image at pixel (i,j) and time t, $I_{i,j,mean}$ is the average of all N values. Speckle variance (SV) imaging has already been shown to be superior to DOCT for 3D vasculature in skin of a nude adult mouse [42, 43]. SV imaging is sensitive to both transverse and the axial components of blood flow. SV imaging has also been demonstrated to be able to quantify flow velocity [44-46].

1.4 Imaging of embryonic development with OCT

Embryos of various vertebrates are widely used to understand different aspects of human development and associated congenital diseases. The mouse is particularly an attractive model to study mammalian development, as they or not only physiologically similar to humans, but recent technologies have enabled the creation of wide variety of

models for human diseases. Mice models for ocular diseases [47], hearing disorders [48], skeletal abnormalities [49], neurological disorders [50], neuromuscular disorders [51], cardiovascular disorders [52] amongst many others exist. The other characteristics of mice, which make them attractive for research use, are their size, low maintenance cost, and a relatively quick gestation period of ~3 weeks.

OCT has been widely implemented for embryonic imaging due to its attractive imaging characteristics. One of the earliest application of OCT in embryology was to perform cross-sectional structural imaging in *Xenopus laevis* (South African clawed frog), *Brachydanio rerio* (zebra fish) and *Rana pipens* (American leopard frog) embryos [53]. OCT has been used to monitor the development of organs such as the eye, brain, heart, ear and spine in zebra fish embryo [54]. OCT has also been very popular to study cardiovascular dynamics in different embryos. Boppart et al. compared reconstruction of 3D structure of a non-beating and anesthetized *Xenopus laevis* embryo heart [55]. Mariampillai et al. later demonstrated 4D reconstruction of *Xenopus laevis* embryo heart [35]. 4D reconstructions have also been performed on chick embryo [56, 57] and mouse embryo [58]. Our group has developed protocols for live imaging of mouse embryos *in vitro* and *in utero* conditions using OCT [59-62]. We have demonstrated the possibility of performing longitudinal studies *in utero* conditions for studying different morphological features during mouse embryonic development [62].

Doppler OCT (DOCT) is the functional extension of OCT technology allowing for detection and quantification of flow by analyzing OCT data. With advancements in speeds of OCT systems, DOCT has now widely been implemented to cardiovascular dynamics in animal models such as *Xenopus laevis* [35, 63] and mouse embryo [61].

Besides DOCT, phase contrast method has also been implemented to image flow in zebra fish embryo [41].

1.5 Description of experimental SSOCT system

The system used for the experiments described in this thesis is based on a broadband swept-source laser (Thorlabs, Sl-1325 P16) (Figure 1.7). The swept-source laser has a central wavelength of 1325 nm with a bandwidth of 100 nm. The power of the laser is 12 mW and its sweep-rate is 16 kHz. The MZI-based interferometer comprises of a 90/10 beam-splitter, which directs 90% of the incident power into the sample arm, and 10% into the reference arm. An additional 99/1 beam-splitter is used in the sample arm which directs 99% of the power on to the sample and 1% onto an external MZI clock source, which is required for recalibration of the detected interference data into linear k-space. Two galvos mirrors are placed in the sample arm which is required for transverse scanning of the sample. The back-scattered light from the sample interferes with the back-reflected light from the reference arm which is detected by a dual-balanced InGaAs-based photodetector (Thorlabs, PDB 140C). The raw data detected by the photodetector is digitized by a 14-bit digitizer (AlazarTech) and recalibrated into linear k-space using the external MZI clock. Structural and phase information of the sample are obtained by performing FFT on the recalibrated data. The system has an axial resolution of 9 μm (in air), transverse resolution of 15 μm, and imaging depth of 3 mm (in air). The depth information is always recorded in 512 pixels.

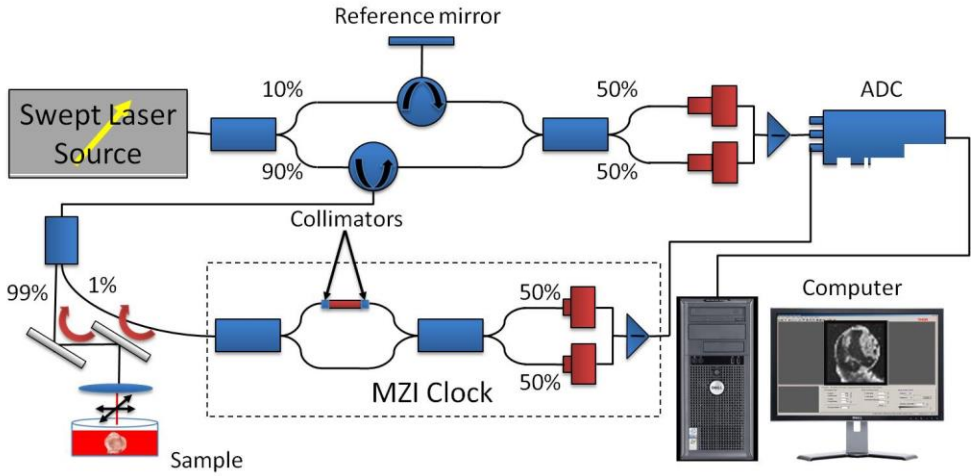

Figure 1.7. Schematic of SSOCT system used for experimental procedures.

The images from the SSOCT system are stored in two file formats, '.IMG' or '.FRG'. All the B-scans from a single recording are stored in a single file. Appropriate B-scan can be reconstructed by reading the header information of the file.

The '.IMG' files stores 8-bit grey-scaled images. They can contain either structural or Doppler information. The structural images are obtained from the magnitude of the FFT of the calibrated data and converted to dB scale. This information is then thresholded based on user input and rescaled to unsigned 8-bit grey-scale values, which is stored in the '.IMG' file. In Doppler images, the phase values of $[-\pi, +\pi]$ radians are represented by [0, 255] in grey-scale, such that 0 radians corresponds to a grey-scale value of 128.

The '.FRG' files stores the calibrated "raw" data in a 16-bit format. The magnitude and the phase information can be retrieved by performing FFT on this calibrated data. The '.FRG' file occupies more hard-disk space, however, it is required for data post-processing using advanced algorithms. Images were recorded as '.IMG' for all experiments where velocity was estimated using DOCT. Images were recorded as '.FRG' for all the experiments where flow was detected using SV imaging.

1.6 Specific aims

1) To characterize the remodeling of the yolk sac vasculature of mouse embryos between E8.5 and E9.5 stages using SVOCT
2) To demonstrate the feasibility of OCT to study the development of the mouse embryo eye by monitoring the volume of the lens and globe volume between E13.5 to E18.5 stages.
3) To demonstrate the advantages of OCT over ultrasound biomicroscopy (UBM) to study the effects of prenatal exposure to alcohol on brain development.

Chapter 2. Characterizing Yolk Sac Remodeling Using Speckle Variance OCT

2.1 Introduction

Congenital cardiovascular diseases (CVD) are some of the most commonly occurring birth defects. More than 5 out of 1000 newborns are affected by CVD each year [64, 65], currently affecting more than a million Americans [66]. Common incidents of CVD occur in the form of holes in the heart septum, more commonly referred to as "hole in the heart", such as atrial septal defect (ASD) [67] and ventricular septal defect (VSD) [68]. Defects in the heart valves, such as stenosis [69], atresia [70], and regurgitation [71] are also common. These diseases primarily affect the blood flow within the heart. More complex CVD occur due to improper development of the heart or defects in the blood vessels connected to the heart [68]. Although CVD can be diagnosed and surgically treated after the birth, the complex mechanisms which lead to these diseases and their effects are not fully understood. Gaining insight into these mechanisms may allow for the treatment and/or prevention of CVD during developmental stages.

A number of studies on cardiovascular development have been performed on different animal models including zebra fish [72-74], *Xenopus laevis* [75-77] and avian embryos [78, 79]. However, mice embryos are preferred as a model for CVD, since they are mammals and their cardiovascular development is very similar to that of humans, and wide availability of mouse mutants associated with human birth defects and diseases [52, 80-82].

The cardiovascular system is the first operational organ system to develop in a mammalian embryo. A primitive linear heart tube is formed from cardiac progenitors, which are derived from the mesoderm at the midline, and begins to beat by the time the

embryo is approximately E8 [83]. During this period, a circulatory network is establishing comprising the heart, dorsal aorta, yolk sac plexus, and sinus venosus [84, 85]. At E8-10, significant changes occur in the morphology of the embryo including the vascular network. During this stage, the yolk sac vasculature also undergoes significant remodeling [23]. Previous studies have shown that blood flow plays an important role for normal development and remodeling of the heart and the vasculature [82, 86, 87].

Several studies have also shown that lack of blood flow can lead to defects in heart and vasculature development [88-91]. It has also been established that normal cardiovascular development depends not only on the gene regulation, but also on the mechanical forces induced by blood flow [92]. The shear stress of blood flow is thought to be responsible for shaping blood vessels and heart chambers [86]. Therefore, lack of vasculature, abnormal vascularization, and other vascular defects are an indication of CVD, which are often fatal to embryos [86]. Hence, it is of immense importance and interest to follow the origin and developmental processes of embryonic vasculature as it can elucidate reasons for abnormal cardiovascular development at early stages of embryonic development.

2.2 Imaging modalities for vasculature detection

Blood vessel imaging techniques have become common clinical procedures to diagnose various ailments. The normal flow of blood in the vessels is often altered by conditions such as ischemia, which results in local thinning of a blood vessel or aneurysm, which results in local bulging of a blood vessel. Autoradiographic techniques have been successful in imaging cerebral blood flow (CBF), but the use of ionizing beams, such as x-rays or gamma rays, make this technique potentially dangerous to living

tissues [93]. Delineating of blood vessels is also a major challenge using autoradiographic techniques. Computerized tomography (CT) angiography is another invasive modality which has mainly been used to image blood vessels in the human brain [94, 95]. Positron emission tomography (PET) has also been employed for blood vasculature imaging [96]. However, PET imaging is based on positron emission from the radioactive isotopes which have to be injected in the blood stream to image the vasculature. Magnetic resonance angiography (MRA) techniques, which are based on magnetic resonance imaging (MRI), employ the use of contrast agents which have paramagnetic properties. MRA imaging is based on the rate of change of concentration of the contrast agents [97]. Angiogram techniques have been very successful in providing comprehensive 3D images of the blood vasculature. However, they normally have a resolution limit of around a few hundred microns, which is not capable of visualizing of small blood vessels. Complex image processing algorithms are also often used for accurate 3D reconstruction of vasculature using angiographic modalities [98].

Ultrasound imaging (ultrasonography) is a noninvasive imaging modality which uses echolocation to perform imaging of tissues and even whole organs. Ultrasonography uses ultrasound waves (1-20 MHz) produced and received by an ultrasonic transducer. The 2D/3D images are reconstructed by analyzing the echoes from tissues (acoustic boundaries) located at different depths in the body. Ultrasonography has been especially popular in obstetrics [99]. It is used regularly to monitor the growth of a human fetus. Doppler Ultrasonography, based on the Doppler effect, can be used for detection and quantification of blood flow profiles in the vessels. Ultrasonography has been shown to provide useful information in attempts of early detection of various

congenital diseases, using both structural and Doppler information [100-102]. Although Ultrasonography has an excellent imaging depth and has been successful in monitoring growth of a human embryo, its resolution is in the order of a ~ 100 microns [103], which is insufficient for imaging small capillaries in developing embryos, such as a mouse embryo.

Optical imaging modalities have the advantage of increased resolution and contrast over non-optical methods. Laser Doppler flowmetry (LDF) and laser speckle contrast analysis (LASCA) are two optical imaging techniques which have been used to detect blood flow [104, 105]. Although these imaging systems are simple to implement, they can obtain only 2D flow information. Photoacoustic tomography (PAT) combines the advantages of both optical and ultrasound imaging to obtain both 2D/3D structural and functional images of biological tissues [106-109]. PAT retains the optical contrast of optical imaging and the imaging resolution of ultrasound imaging. However, the resolution of PA images is limited to ~50-100 μm and imaging speed is in the order of a few Hz. On the other hand, confocal microscopy [110] can produce very high resolution (< 1 μm) images and has been extensively used in imaging of tissues and cells including vasculature of a mouse embryo [92, 111-114]. While confocal microscopy has revolutionized optical imaging at subcellular resolution, the major disadvantages of this method for imaging of live tissues and cells are the requirement of using fluorophores and limited imaging penetration depth inside the tissues which is in the order of 100 microns. Optical projection tomography (OPT) utilizes analysis of optical projection of scattered light on to an imaging detector -- much similar to CT [115]. OPT has been applied in various fields including imaging of complete vasculature in a fixed E8-10

mouse embryo using [85]. The major disadvantage of OPT is the requirement for labeling of tissues of interest and requirement for tissues to be relatively transparent.

Optical coherence tomography (OCT) is a noninvasive imaging technique that allows for real-time structural and functional 3-D imaging with a resolution of about 2-20 μm and an imaging depth of a few millimeters [1]. OCT relies on the natural optical tissue contrast and does not require the use of contrast agents. These features have made OCT an attractive tool for live embryonic imaging in a mouse [57, 59, 116] as well as other animal models [57, 117]. Usually, the vascular structure is reconstructed based on Doppler OCT analysis of the blood flow [118-121]. The major drawback of the Doppler OCT for blood flow analysis and reconstruction of vascular structure is its insensitivity to transverse component of blood flow, which prevents Doppler OCT visualization of vessels perpendicular to the scanning laser beam. Another disadvantage of the Doppler OCT is its dependence on phase stability of the system. To address this point, OCT systems with higher phase stability have been developed [17]. Recently, optical micro-angiography (OMAG) has been employed to image vasculature in adult mouse brain [37]. Even though, OMAG has a higher sensitivity to flow than Doppler OCT, its inability to detect transverse flow is still a drawback. Phase contrast method has been implemented to detect both components of blood velocity [41]. This method is however subjected to phase sensitivity of the system. An alternative approach is from statistical analysis of time-varying speckle in the OCT structural images [42, 43, 46]. Speckle arises in OCT structural image as a consequence of using a coherent laser source [26].

In this study, we tested application of SV OCT analysis for 3-D reconstruction of the vasculature in live mouse embryos cultured on the imaging stage. The SV OCT analysis was compared to the Doppler OCT method, demonstrating its advantage to visualize the vessels in the transverse orientation. The analysis is focused on E8.5 and E9.5 stages, as these stages represent changes in vascular network within first 24 hours after the beginning of the blood circulation. Visualization of the vasculature during this period is of high interest in the embryology research to study the effect of genetic manipulations and pharmacological agents on the cardiovascular development.

2.3 Flow model experiments

To demonstrate the advantages of using SV OCT imaging over Doppler OCT for 3D vasculature detection, experiments with flow models were designed. Whole milk flowing through a capillary tube is used as a model for blood flowing through a vessel. Milk is a colloid of fat, proteins, salts, and other compounds that make it optically inhomogeneous. Due to its optical properties [122, 123], milk is frequently used as tissue models in many studies [124, 125].

2.3.1 Experimental setup

A SSOCT system (described in section 1.5) was used for imaging milk flowing through a capillary tube under preset conditions. A calibrated syringe pump (Harvard apparatus 22) was used to adjust the flow rate of milk through the capillary tube. Milk was contained in a 3 ml syringe (BD), with an internal diameter (ID) of 8.66 mm, and connected to a capillary tube (ID ~ 490 μm) via plastic pipes. After leaving the capillary tube, milk was drained into a beaker. Prior to initiating the experiment, the capillary tube and the plastic tubes were completely filled with the milk. To minimize phase noise due

to operational vibrations, the syringe pump was placed on a separate table with no direct physical contact with the optical table where the whole experimental setup was assembled. SSOCT data were recorded only after the flow in the syringe was stabilized.

To compare DOCT and SV imaging, the milk was pumped through the capillary tube at fixed flow rates (0, 0.1, 1, 2, 3 and 4 ml/h) while the tube was held at different inclinations with respect to the laser beam (70°, 74°, 80° and 89°). The laser beam was scanned at the center of the length of the capillary tube. To precisely determine the angle of inclination, a B-scan was acquired longitudinal to the capillary tube as shown in Figure 2.1a. The angle was determined by calculating the angle made by the top surface of the capillary tube from the SSOCT structural images.

Since the measurements were made at the center of the length of the capillary tube, the flow of milk was assumed to be laminar. The average flow velocity of milk in the capillary tube was calculated by dividing the volumetric flow rate by the cross-sectional area. Using the value of 490 μm as ID of the capillary tube, flow rates of 0, 0.1, 1, 2, 3 and 4 ml/h gives the flow velocities of 0, 0.148, 1.48, 2.96, 4.44 and 5.92 mm/s, respectively by using the relation,

$$Volume\ flow\ rate = Cross\ sectional\ area\ \times Velocity. \tag{2.1}$$

2.3.2 Data processing

Figures 2.1a and b represent typical SSOCT images recorded in the longitudinal and transverse cross-section directions of the capillary tube containing milk. The inclination of the capillary tube with respect to the laser beam can easily be calculated by determining the slope of the top surface of the capillary tube, as shown in Figure 2.1a. In

the presented image, the angle of inclination was determined to be 80°. Similarly, the angle was precisely determined for data recorded at other inclinations.

From Doppler images, phase difference values (in radians) using equation 1.10, were used to estimate flow velocity using equation 1.11. A DOCT image is conventionally represented as a color-coded image to distinguish between opposite flow directions. To represent the grey-scaled Doppler images as color coded RGB images, grey-scaled values of [0-127] are represented as [255-0, 0, 0] in RGB scale such that $-\pi$ radians is represented by a bright red color. Grey-scaled values of [128-255] are represented as [0, 0, 0-255] in RGB scale, such that $+\pi$ radians is represented by bright blue color. Grey-scaled value of 127 appears as black in RGB scale. SV images were reconstructed using equation 1.13.

2.3.3 Results

As one can see from Figure 2.1, instead of a uniform intensity pattern, the milk region of OCT image/signals is filled with random bright and dark spots caused by previously described speckle effect. The 1D profile (A-scan) corresponding to the center of the capillary tube is presented in Figure 2.1c. Strong speckle-modulation of the OCT signal is clearly visible in this graph.

The performance of DOCT at different angles and at different velocities is demonstrated in Figure 2.2. It can be clearly seen from Figure 2.2a, that even at a high velocity of 5.92 mm/s, DOCT is unable to detect flow in the capillary tube at angle of 89°. However, at inclinations of 74°and 70°, phase changes have increased dramatically causing phase wrapping as demonstrated in Figure 2.2b-c. The flow velocities are difficult to compute if the phase wraps unless phase unwrapping algorithms are used. A

black band can be observed in both Figures 2.2b and 2.2c between the transition from blue region and red region. This band is created due to averaging of phase jumps between $+\pi$ and $-\pi$, caused by phase wrapping. Figure 2.2d demonstrates that, at an angle of 70° flow velocity of 2.96 mm/s can be detected and quantified, since there are no phase jumps. It is seen from Figure 2.2e that a velocity of 0.148 mm/s cannot be detected at the angle of 70°.

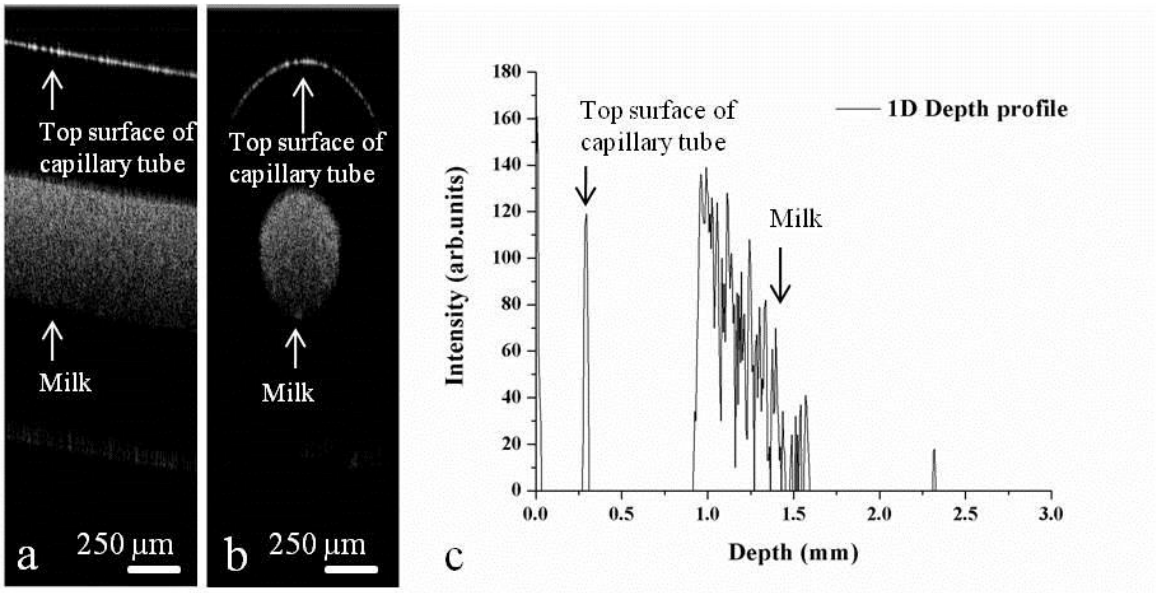

Figure 2.1. Structural images of milk in a capillary tube at 80 degrees inclination. (a) Longitudinal cross-section of capillary tube. (b) Transverse cross-section of capillary tube. (c) 1D plot at the center of capillary tube. [126].

The inability of DOCT to detect low axial flow components, phase wrapping at high velocities, and inability to detect velocities at close to 90° prompts for development of alternative solutions. A speckle variance algorithm (Equation 1.13) is one such solution, which can be implemented to efficiently detect both the axial and transverse components of flow. To compare the performance of SV imaging over DOCT, the SV algorithm was implemented on the same data sets as that used for DOCT (Figure 2.2). The obtained results are presented in Figure 2.3. It is clear from the presented images that

SV imaging is capable of detecting the flow in milk irrespective of the angle or the absolute velocity of the flow. For all the images, a suitable display threshold was chosen so that the dynamic scatterers are separate from the static scatterers. For example, a higher display threshold was chosen for data shown in Figure 2.3a due to high variance noise caused by saturation of the photodetector due to strong reflection of light at the center of the capillary tube as the angle is almost 90°. Figures 2.3a-e demonstrates that SV imaging is capable of imaging flow of milk in the capillary tube irrespective of the magnitude of velocity or the angle of flow. A careful comparison between Figures 2.2 and 2.3 reveals that the region of milk detected by SV imaging is a slightly larger than that detected by DOCT. This could be explained by inability of DOCT to detect low flow magnitude near the edges of the capillary tube. These results suggest that SV imaging will be more useful to perform 3D vasculature detection compared to DOCT especially when the blood flow has low axial component.

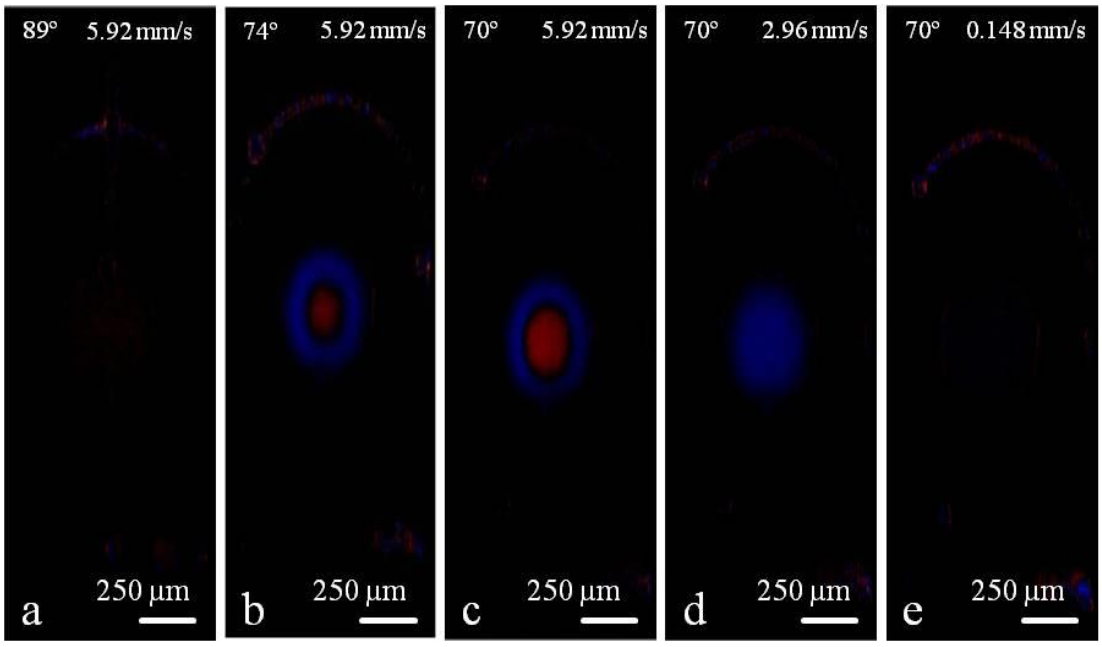

Figure 2.2. DOCT images of milk in a capillary tube at different angles at various velocities of flow. (a) 89° at 5.92 mm/s. (b) 74° at 5.92 mm/s. (c) 70° at 5.92 mm/s. (d) 70° at 2.96 mm/s. (e) 70° at 0.148 mm/s. [126].

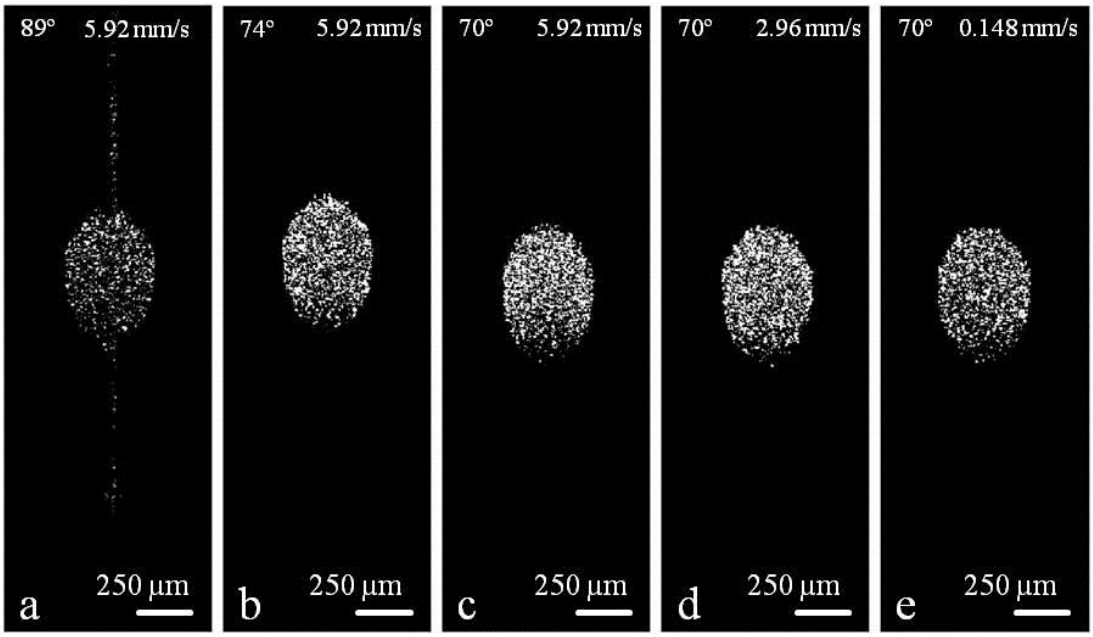

Figure 2.3. Speckle variance images of milk in a capillary tube at different angles at various velocities of flow. (a) 89° at 5.92 mm/s. (b) 74° at 5.92 mm/s. (c) 70° at 5.92 mm/s. (d) 70° at 2.96 mm/s (e) 70° at 0.148 mm/s. [126].

2.4 Detection of 3D vasculature using speckle variance (SV) imaging

2.4.1 Animal model

Wild type CD-1 mice were mated overnight and monitored for vaginal plugs every day. The presence of a vaginal plug was recorded as E0.5. At the desired stage, the pregnant female was sacrificed and the embryos were dissected with the yolk sac intact, on a heated dissection station to 37°C in a medium consisting of 89% DMEM/F12, 10% FBS, 1% Pen-strep solution (Invitrogen, Grand Island, New York). Freshly dissected embryos were transferred to an incubator set to 37°C and 5% CO_2, and imaged within 6 hours after the dissection. The medium assists in maintaining the viability of the embryos during imaging period.

2.4.2 Experimental procedure

For 3D vasculature imaging experiments, the Petri dish containing the embryo was placed on a linear translation stage (LTS) (STANDA) during imaging. The LTS has a minimum step increment of 1.25 µm and capable of moving at a minimum velocity of 20 µm/s. To perform SV imaging, structural images comprising of 256 A-scans or 512 A-scans were acquired at 51 fps or 28 fps. 2D scanning was performed using galvos. The LTS is used for data acquisition in the 3rd dimension. During 3D data acquisition, the stage was translated at a rate of 20 µm/s. For DOCT, 2D imaging was performed by scanning the galvos for either 512 or 1024 A-scans. The SSOCT system described in section 1.5 was used for imaging.

2.5 Results

Monitoring the development and remodeling of the blood vasculature between the stages when mouse embryo is E8.5 and E9.5 can assess the course of cardiovascular development. This section attempts to reconstruct 3D vasculature of a mouse embryo during these stages using both DOCT and SV imaging. To generate 2D SV images, the structural images were de-noised using a suitable threshold and the resulting image was smoothed using a median filter of size 2×2, prior to implementing the SV algorithm. Smoothing the images minimized intensity fluctuations caused by local refractive indices changes within the mouse embryo, at the cost of losing small sized speckles. Hence, the median filter size should be chosen carefully. For 3D SV volumes, an additional median filter of size 2×2 was used in the transverse plane to minimize noise.

To test the capabilities of both the algorithms for detection of blood vessels, 50 B-scans were acquired at the same transverse location of E9.5 mouse embryo. SV images

were acquired using Equation 1.13, with N = 50. The structural image of embryonic yolk sac shown in Figure 2.4a reveals the presence of three blood vessels as indicated by the white arrows. It is noticed from Figure 2.4b, that the DOCT image detects the presence of only two out of the three vessels present in the imaging area. On the other hand, the SV image depicted in Figure 2.4c detects the presence of all the three vessels. The results indicate the limited applicability of DOCT for vasculature detection. This is due to the inability of DOCT to detect flow with low axial component. SV imaging appears to be a more promising tool for 3D vasculature detection. Both DOCT image and SV image show a presence of signal outside the blood vessels. This noise is caused by bulk tissue movement (BTM) as a result of the heart beating and/or local refractive indices changes.

To test the capability of SV imaging for 3D vasculature detection, continuous B-scans were acquired over a distance of 3.33 mm with a E9.5 mouse embryo. The LTS was being translated at a rate of 20 µm/s over a distance of 3 mm. The total data acquisition time was 2 minutes and 30 seconds. The B-scans were comprised of 256 A-scans to maintain a high frame rate of 51 fps. A single 2D SV image was constructed from 10 2D structural images by applying Equation 1.13, using N = 10. Since the frame rate is 51 fps and the linear stage is being translated at 20 µm/s, the stage would have translated by an amount of ~ 4 µm during the acquisition of 10 B-scans, which is below the transverse resolution of the system. Hence, the embryo was being assumed to be scanned roughly over the same transverse region. As a result, the variance detected from the blood vessel was assumed to be caused by time varying speckles instead of structural changes caused due to translation of the LTS. A 3D SV volume was constructed by grouping all the resulting 2D SV images and using Thorlabs 3D Viewer for volume

reconstruction. The top view of the resulting structural and SV 3D volumes are presented in Figures 2.5a and b, respectively. The ability of SV algorithm to separate the dynamic scatterers in the blood vessels in the yolk sac from the static scatterers can be observed by comparing Figures 2.5a and b. Figure 2.5b presents the yolk sac vasculature which includes major vessels and small branching capillaries.

Between E8.5 and E9.5 stages, the embryonic cardiovascular system undergoes significant changes [111]. At E8.5, blood circulation begins and the yolk sac vasculature forms an interconnected structure with vascular branches of about the same size (vascular plexus). By E9.5, the shear stress generated by the blood flow facilitates the remodeling of the vascular plexus into more mature branching hierarchical network. Live analysis of the vascular remodeling is important for understanding the role of mechanical factors in cardiovascular development. To assess if the SV OCT method can be used to visualize these changes, we analyzed the yolk sac vasculature in E8.5 and E9.5 embryos, as depicted in Figure 2.6. At both stages, the vasculature is clearly visible. As expected, there is an apparent morphological difference between the primitive vascular plexus at E8.5, presented in Figure 2.6a, and the remodeled hierarchically branching vascular network at E9.5, shown in Figure 2.6b. For data acquisition at E8.5, the stage was translated for a distance of 1 mm, at a rate of 20 μm/s. Total acquisition time was 50 seconds for 256 A-scans fin each B-scan with a range of 1.67 mm. Similarly, for data acquisition at E9.5, the stage was translated for a distance of 3 mm at 20 μm/s. Total acquisition time was 2 minutes and 30 seconds for 256 A-scans in each B-scan with a scanning range of 3.33 mm. These results demonstrate that SV OCT can potentially be used for imaging vascular remodeling in the mouse embryonic yolk sac.

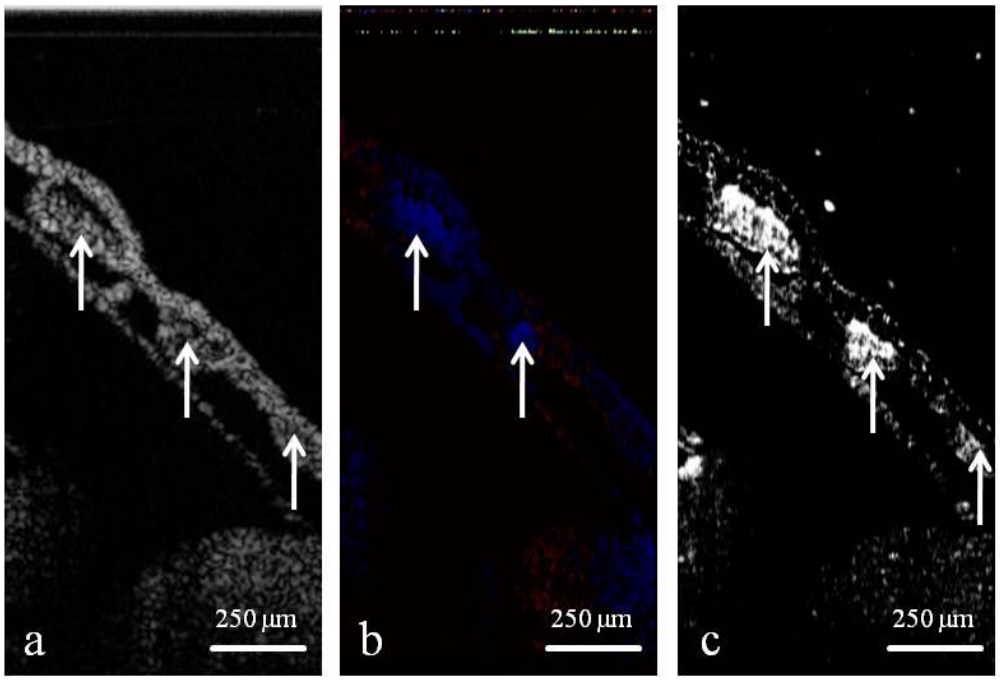

Figure 2.4. Yolk sac blood vessels of E9.5 mouse embryo. (a) Structural image indicates the presence of three blood vessels (b) DOCT image indicates the presence of two blood vessels. (c) SV image indicates the presence of three blood vessels. [126].

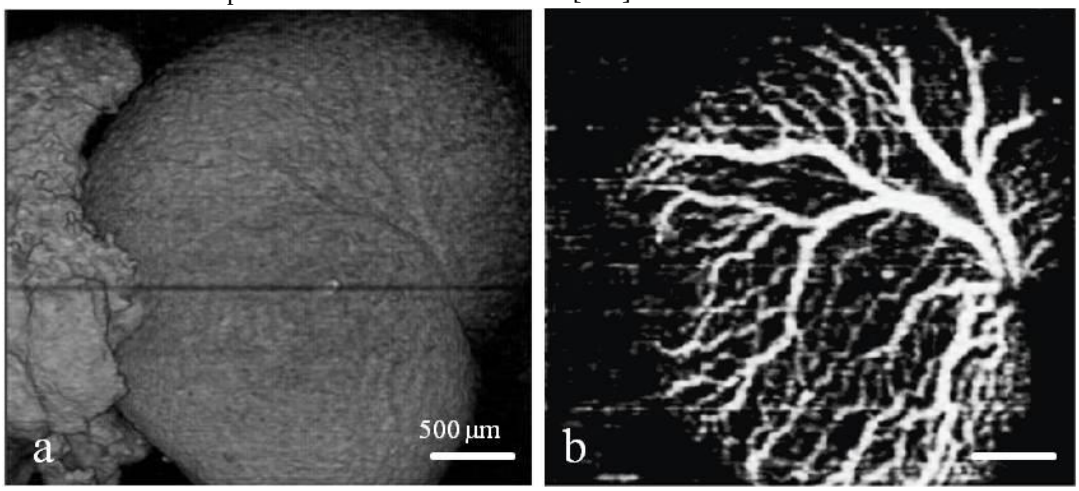

Figure 2.5. Top view of 3D reconstruction of the yolk sac of E9.5 mouse embryo. (a) Structural image. (b) SV image showing the presence of yolk sac vasculature. Scale bar represents 500 µm. [127].

To test the capability of reconstructing embryonic vasculature, 3D volume of brain of an E8.5 mouse embryo was acquired. The images were acquired by scanning over a region of 0.86×0.86 mm^2 comprising of 512×512 A-scans. Both DOCT and SV imaging were used for detection of the brain vasculature, for comparison. The vascular

structure reconstructed using DOCT shown in Figure 2.7a is similar to the one reconstructed using SV imaging shown in Figure 2.7b. This suggests that DOCT and SV imaging perform equally well when blood flow has a significant axial component, which is typical in embryonic vessels

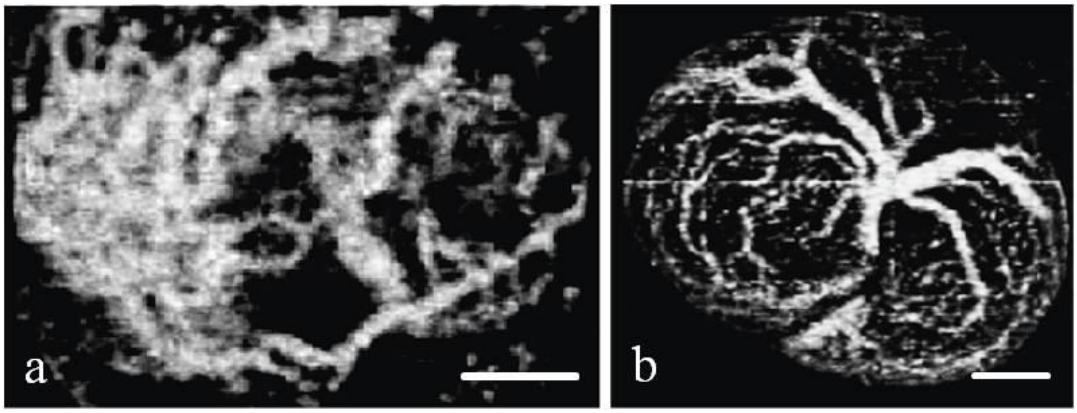

Figure 2.6. Top view of 3D reconstruction using SV imaging of the yolk sac vasculature. (a) Non-remodeled vasculature (vascular plexus) of the embryonic yolk sac at E8.5. Scale bar represents 250 µm. (b) Remodeled yolk sac vasculature at E9.5. [127].

In contrast, in the embryonic yolk sac the vasculature is flat and is nearly perpendicular to the scanning beam. To compare performance of DOCT with SV imaging in such cases, 3D volumes were obtained from yolk sac of the embryo at E9.5. SV imaging shown in Figure 2.7d is much more efficient in visualizing the vasculature than the DOCT shown in Figure 2.7c. Figures 2.7c and 2.7d correspond to the vascular network branching from the vitelline artery of the embryo at E9.5. Even though this part of the vasculature exhibits higher blood flow then the rest of the yolk sac, only a few major vessels are visible in the DOCT reconstruction (Figure 2.7c). The branching capillaries and the vessels in the central part, where the yolk sac is perpendicular to the laser beam, are not detectable. The corresponding SV OCT reconstruction (Figure 2.7d) shows both large vessels and small capillaries regardless of the flow direction. These results demonstrate that the SV OCT imaging provides more accurate 3-D visualization

of the vasculature then the DOCT method, since DOCT relies on the axial component of the blood flow whereas SV OCT is not sensitive to the flow direction.

Although SV imaging has its advantages over DOCT for 3D vasculature reconstruction, presently, a critical disadvantage of SV imaging is intensity fluctuations underneath blood vessels caused by changes in refractive indices in the vessels, leading to a shadowing effect [41]. Similar to Doppler OCT, SV imaging is sensitive to high bulk tissue movement (BTM) which causes high inter-frame variance. Imaging systems with high A-scan acquisition speed can be used to ensure a sufficient number of acquired frames for calculating speckle de-correlation while the BTM is negligible [35].

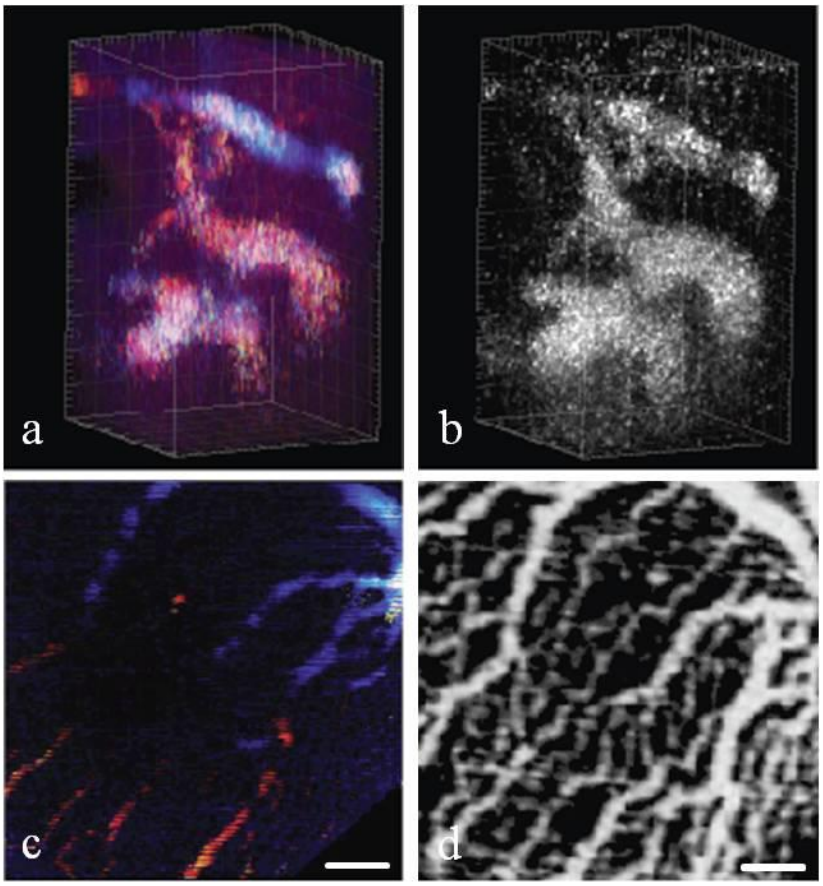

Figure 2.7. (a-b) 3D vasculature in the mouse embryonic brain at E8.5 obtained with DOCT & SV imaging respectively. Major ticks represent 50 µm. (c-d) 3D yolk sac vasculature at E9.5 acquired with DOCT & SV imaging respectively. Scale bar represents 250 µm. [127].

2.6 Conclusions

In this study, we tested application of SV OCT imaging for 3-D reconstruction of the embryonic vasculature in live cultured mouse embryos. Our studies demonstrated that this method can successfully be used to visualize both yolk sac and deep embryonic vessels. Comparison of the SV and the Doppler OCT algorithms demonstrated that SV analysis provides more accurate representation of the vascular structure since it is not sensitive to the direction of the blood flow. This advantage is especially beneficial for imaging of the embryonic yolk sac due to its flat vascular network. This study suggests that SV OCT imaging is a useful tool to study development and remodeling of the vasculature in live mouse embryo culture. Potentially this method can help to advance embryonic cardiovascular research in animal models.

Chapter 3. Studying Eye Development in Mouse Embryo Using OCT

3.1 Introduction

An eye is a highly complex structure and one of the most important sensory organs in a vertebrate. It is composed of three main tissues, namely the cornea, the lens and the retina. The formation of the eye is orchestrated by well-coordinated actions of genes which occur during embryonic development. The development of the eyes in a mouse embryo begins at grastulation when it is organized as a single eye field located centrally in the forebrain. The single eye field then separates during the establishment of the midline. The earliest signs of the eye during development process begin to appear at E8.5 stage when the lateral walls of the diencephalon begin to bulge out to form optic pits. At E9.5 stage, the lens placode comes in contact with the optic vesicle which results in neuroectoderm folding inwards to form the optic cup. The retina arises from the inner layer of the optic cup whereas its outer layer gives rise to retinal pigment epithelium. The lens arises due to the invagination of the lens placode and the cornea is formed when the lens detaches from the surface epithelium [128]. The nutrients required for the development and the differentiation of the eye during embryogenesis, is provided by the hyaloid vasculature.

The causes of several congenital eye disorders have been recognized as due to mutations of key genes during the developmental process. One such example is the point mutation affecting the alternative translation initiation of the gene *Rax*, which causes the *eyeless* phenotype or anophthalmia [129]. The mouse embryos which carry null allele of this gene do not form optic cups and hence do not develop eyes [130]. Similarly, loss of *Six3* or *Shh* genes can prevent the splitting of the eye field resulting in a condition called

cyclopia where the embryo is born with a single eye [131]. *Pax6* gene is one of the most important transcription factors and has been recognized as the master control gene of eye development. One of the earliest mutations of *Pax6* recognized in a mouse results in small in heterozygous mutants, however, the homogenous mutants possess only remnants of ocular tissues and die soon after birth. Several studies using knockout mutants for *Pax6* revealed that *Pax6* is necessary for the formation of lens placode and for the lens; however it is not essential for the formation of the optic cup. Another gene which affects the lens development is the *Pitx3* gene. Mutations in this gene lead to lack of lenses and pupils in mice [132-134]. Similar to humans, *FoxC1* knockout mice have shown to have anterior segment abnormalities [135]. A severely affected mouse mutant, called the recessive *ocular retardation* which is caused by the homozygous presence of mutated *Chx10* gene. This mutant suffers from microphthalmia and possesses a cataractous lens and a thin retina [136]. *Chx10* is essential for repressing *Mitf* which results in maintaining the mammalian neuroretinal identity [137].

Mice have been preferred animal to study human congenital disorders due to availability of wide range of mutant models for human eye diseases. Amongst numerous mutant models, one such is a mouse model for galactose induced cataracts was created by cloning the mouse *Glk1* gene and then disrupting it by gene targeting [138]. Metabolism of galactose was very poor in this mutant model which resulted in galactosemic cataract. DBA/2J mice have been used as model for glaucoma. These mice develop pigmentary glaucoma which involves iris pigment dispersion (IPD) and iris stromal atrophy (ISA) due to mutation in *Gpnmb* and *Tryp1* genes respectively [139]. Transgenic mice for retinoblastoma [140] and intraocular tumors [141] have also been developed.

3.2 Imaging modalities for studying mouse eye development

Traditionally, histology has been used for studying ocular development and diseases [138-141]. Although it has been extremely useful it has several disadvantages such as tissue deformation during fixation and processing, and an inability to provide information in real-time. This makes the approach inapplicable for a number of studies. Imaging tools such as magnetic resonance imaging (MRI) and ultrasound (US) permit longitudinal studies. These methods are noninvasive and can capture real-time 3D, structural and dynamic information.

MRI is a 3D imaging modality which has been used for mouse phenotyping for both *in vivo* and *ex vivo* conditions. The application of MRI for mouse development biology was first developed by Smith et al., where they could obtain 3D images under *ex vivo* conditions with a resolution of 20-50 μm [142]. High-resolution MRI has also been used to create a 3D digital mouse atlas for fixed embryos from E6 to E15.5 [143]. MRI is robustly designed for imaging anatomical structures in large animals and humans; however, it faces significant technical challenges for imaging embryonic and neonatal mouse due to the limited resolution. Longitudinal studies *in utero* conditions to study mouse embryo development have been demonstrated. However, a resolution of only 100 μm was achieved for such studies [144]. An application of MRI in ocular development was also demonstrated using a high-resolution small animal MRI system, however its application was restricted to analyzing postnatal development [145]. The resolution of all MRI systems is dependent on the SNR and the scanning time. While *ex vivo* MRI imaging of fixed mouse embryos has previously been performed with up to 20 μm of resolution, *in utero* imaging [144] only allows for resolution of about 100 μm; besides,

and imaging time (~ 2h) is required to achieve sufficient SNR . Another major limitation of MRI systems is poor contrast due to minimal differences in MR relaxation properties from immature and undifferentiated cells and tissues which restricts its application in mouse embryonic imaging [146].

High-frequency US or ultrasound biomicroscopy (UBM) is widely used in mouse embryo research. UBM transducers typically operate at 40-100 MHz range which results in higher resolution compared to the transducers which are used in clinical settings and that operate in the 2-15 MHZ range. UBM has been demonstrated the capability of *in utero* imaging of early brain development of mouse embryo [147]. It has also been applied for noninvasive analysis of cardiovascular development and measuring blood flow in mouse embryos [148]. Measurements of the anterior chamber using UBM were performed to study the development of glaucoma in mutant mice at different ages ranging from 2 to 30 months [149]. Additionally, the technology has been utilized to monitor the development of ocular tissues at different stages of embryonic development and regression of hyaloid vasculature in mice [150, 151]. High frequency ultrasound imaging can achieve axial resolution of up to 30 μm, which is not sufficient to resolve some structures including hyaloid vasculature; in addition, it lacks sufficient contrast to distinguish between different biological tissues due to their weaker acoustic scattering compared to their optical scattering [152] .

In this study, we performed quantitative assessment of mouse embryonic ocular structures at different stages from E13.5 to E18.5 *in utero* with OCT. Acquired measurements were correlated with previously reported values obtained with UBM. Potentially, this approach can be used to assess embryonic ocular growth in mouse

mutants with eye abnormalities and to study the effect of toxicological and pharmacological agents on embryonic eye development.

3.3 Experimental setup

The swept-source OCT (SSOCT) system which has earlier been described in section 1.5 was used for imaging. This system was used to obtain 3D volumes of mouse embryonic eyes from E13.5 to E18.5.

3.3.1 Mouse manipulations

All animal manipulation procedures described here were approved by the Animal Care and Use Committee of the University of Houston. The animal detailed manipulation protocol is described in [62]. Briefly, the pregnant mice at the desired stage were anesthetized using isoflurane by inhalation. The anesthetized mouse was placed on a heating platform maintained at 37° C during the entire procedure. An electrical razor was used to remove the abdominal fur at the incision site. An incision of ~1-2 cm was made on the abdomen to expose the uterine horn for imaging. OCT imaging of the embryonic ocular structure was performed through the uterine horn. After the imaging was complete, the mouse was immediately sacrificed. From every litter, 2-3 embryos were imaged. At least five embryos from each stage were analyzed. Measurements were made at E13.5 to E18.5.

3.4 Eye volume measurement

To make volumetric measurements of the eye, it was assumed to be of oblate spheroid shape [150]. An oblate spheroid is a rotationally symmetric ellipsoid. Its transverse plane, which contains the major axes, is circular and its axial planes which

contain a major and the minor axes are elliptical. The volume of an oblate spheroid is given by,

$$V = \frac{4}{3}\pi a^2 c, \tag{3.1}$$

where V is the volume, *a* and *c* are the radii of major and minor axes, respectively. The refractive indexes of ocular tissues were assumed to 1.4 [153]. The major and the minor axes of the eye lens and the eye globe can be obtained from 2D cross-sections which contain them. Since orienting embryos in utero for imaging is a challenging task, and the major and minor axes of the embryo eye can be randomly located within the acquired data set. This restricts the possibility of directly obtaining the major and minor axes from the acquired data set. To overcome this problem, a MATLAB based graphical user interface (GUI) code was designed which could perform rotation of 3D data set.

3.4.1 GUI for 3D rotation

The GUI used for 3D rotation is displayed in Figure 3.1. The GUI loads the entire 3D image data into memory. By convention, the depth direction is referred to as the Z axis, the primary transverse direction of a B scan is the X axis and the 3rd direction is the Y axis. The GUI enables the viewing of 2D cross-sectional slices from each of the three planes, namely, the XZ, YZ and the XY planes by selecting the appropriate radio button. Different slices at a particular plane can be viewed by changing the 'location' slide bar. An individual plane can be rotated by moving the 'tilt' slide bar in the GUI. 3D rotation is performed by rotating individual planes. Since only one 2D cross-section is visualized at a single instant, the underneath code first creates an empty matrix which will hold the rotated cross-sectional image, with appropriate dimensions (rounded off to nearest integer) depending on the size of the original image and the rotation angle. For example,

if the size of the original image is 512×512 and the rotation angle is 45 degrees, then the size of the empty matrix which holds the rotated matrix will be 724×724 (512×$\sqrt{2}$). The data in the matrix is then filled up with values from the original 3D data set, by performing inverse rotation of the coordinates of the empty matrix to obtain the corresponding coordinates from the original 3D data set.

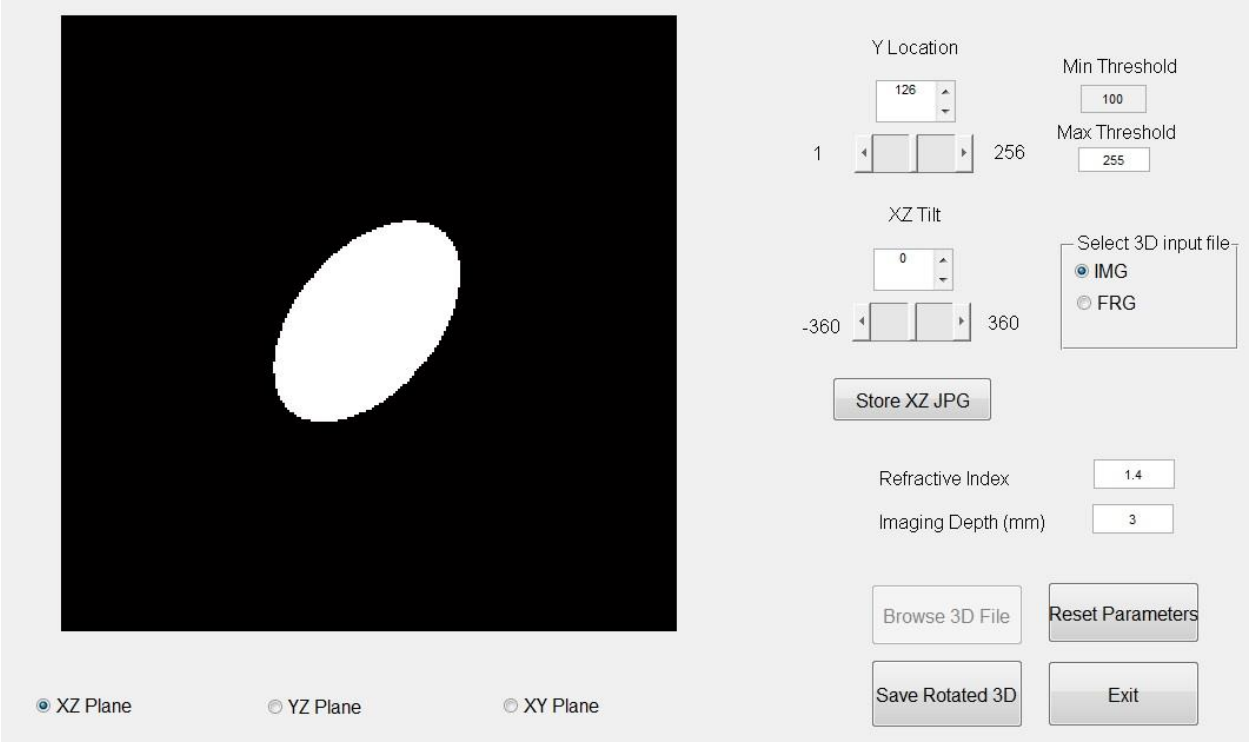

Figure 3.1. MATLAB based GUI used for 3D rotation.

To validate the rotation procedure using the GUI, an oblate spheroid was simulated such that it was rotated by 45º in XZ plane, 30º in YZ plane and 15º in XY plane. The 3 cross-sectional planes of the rotated oblate spheroid are presented in Figure 3.2. For an oblate spheroid which has not been rotated, it should appear circular in XY plane and elliptical in XZ and YZ planes. However, it is clear from the images presented in Figure 3.2 that all the planes look elliptical due to rotation. To perform 3D rotation, the rotated oblate spheroid in the image file was loaded onto the GUI. At every plane, the

slice where the ellipse appeared the largest was selected, following which, the ellipses were rotated until they aligned with respect to the 3D volume (the red line is parallel or perpendicular to the green line). The result of the rotation is presented in Figure 3.3. It can be seen that XZ and YZ planes (Figures 3.3a&b) appear elliptical, whereas the XY plane (Figure 3.3c) appears circular. It should be noted that the individual images presented in Figure 3.3 are in scale but have been cropped and resized to match each other's dimensions. It can be concluded from the results presented in Figures 3.2 and 3.3 that the GUI can be useful for performing 3D rotation.

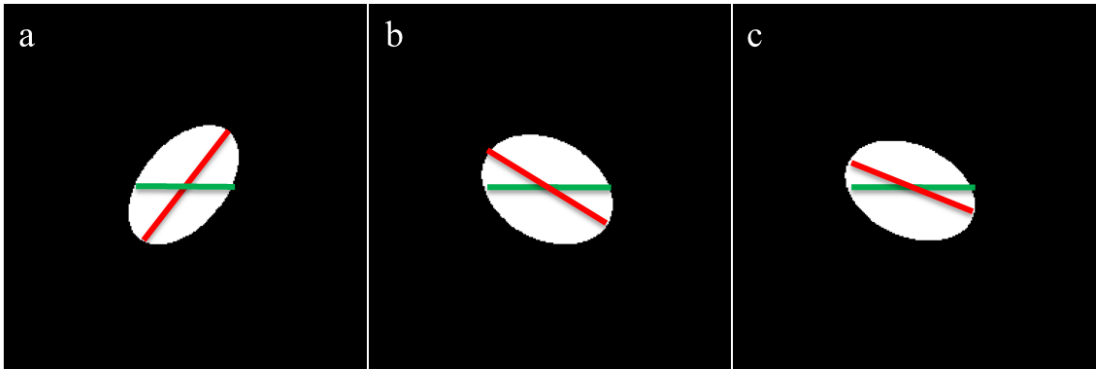

Figure 3.2. Simulation of a rotated oblate spheroid (a) XZ plane rotated at 45º (b) YZ plane rotated at 30º (c) XY plane rotated at 15º. The red line describes the original tilt and the green line represents the intended tilt.

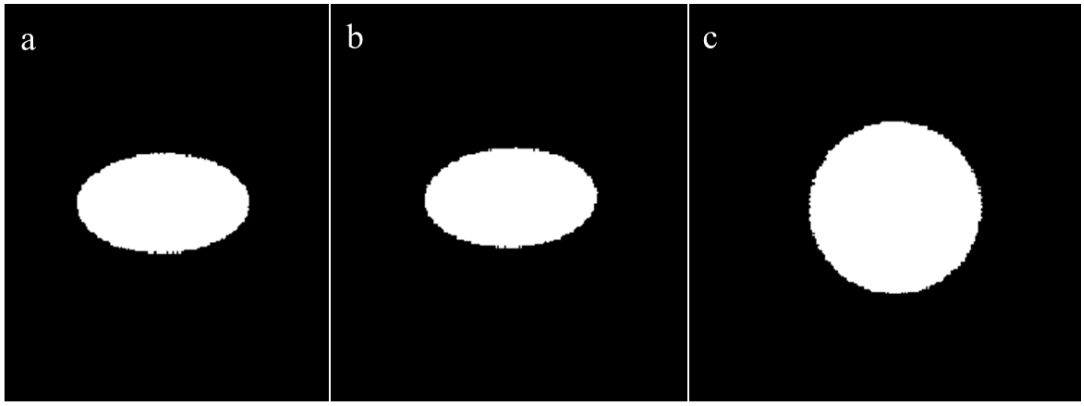

Figure 3.3. Rotation of the simulated oblate spheroid using GUI. Note: The images are in scale but have been cropped.

3.4.2 3D rotation of mouse embryonic eye

Data sets containing 3D images of the mouse embryonic eye were loaded to the GUI individually. At every cross-sectional plane, the slice where the eye appears the largest was selected and then rotated so that the optic axes of the eye aligns with the 3D volume, similar to procedure described above. Once the images were rotated to correct the alignment, ImageJ software was used to measure the diameters along the major and minor axes. The volume of the eye lens and the globe was determined using formula 3.1.

3.5 Results

Typical OCT images containing embryonic eyes acquired *in utero* at different stages are presented in Figure 3.4. The whole eye is within the imaging depth of the OCT even at the latest imaged stage (E18.5), and there is sufficient contrast between the tissues. Different embryonic ocular structures are easily identifiable (as labeled). The difference in size and morphology is clearly distinguishable between the developmental stages, as expected.

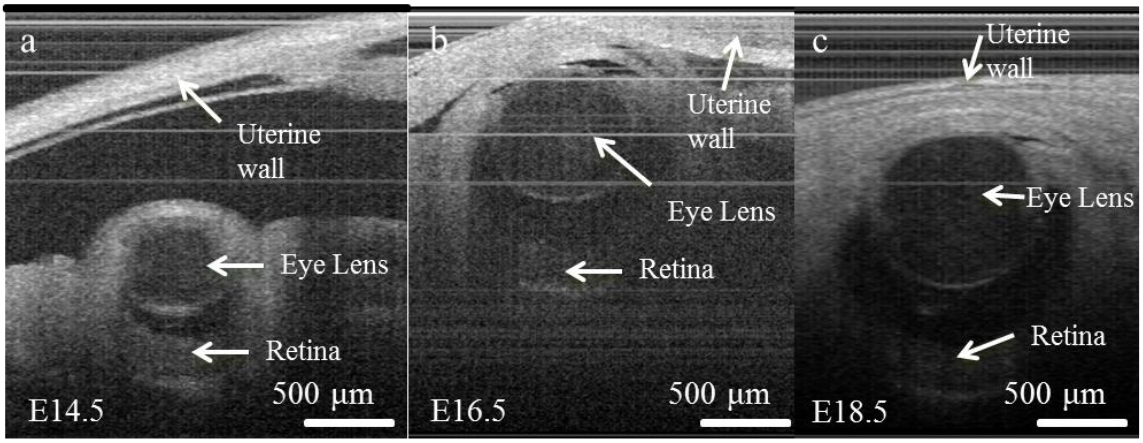

Figure 3.4. 2D OCT images through the eye in utero at different stages of embryonic growth.

To orient the OCT data sets along the optic axes of the embryonic eye for measurement, we developed and applied a Matlab based GUI code. The effect of 3D rotation of the mouse embryo eye data set is demonstrated in Figure 3.5. Figures 3.5(a, c)

show the OCT axial and transverse cross-sections of the eye prior to application of the code, while Figures 3.5(b, d) demonstrate corresponding cross-sections after the OCT data set rotation.

The major and minor axes diameters were measured from the oriented 3D data sets using the ImageJ software. To estimate the volume of the eye, the shapes of the eye lens and the eye globe are assumed to be oblate spheroid. An oblate spheroid is circular in its transverse cross-section (by our convention, xy plane) and elliptical in its axial cross-sections (by our convention, xz or yz plane), with its major axes (by our convention, x and y axes) along the transverse directions and its minor axis along the axial direction (by our convention, z axis). Since an oblate spheroid is circular in its transverse direction, the measurement of the major axis diameters along the x-axis and the y-axis should be the same. It can be observed from Figure 2b that the axial cross-section of the eye lens and globe is elliptical and the circular nature of the transverse cross-section is apparent in Figure 3.5d. To further validate the assumption of oblate spheroid shape, the major axis diameter from both the x-axis and the y-axis (transverse axes) of the eye lens and globe at different growth stages were measured and presented in Figures 3.6a and 3.6b, respectively. The slope of 0.93 with R^2 (coefficient of determination) value of 0.87 for the eye lens and slope of 0.92 with R^2 value of 0.93 for the eye globe implies that the diameters of major axes in the transverse direction are similar, which justifies the assumption that the entire eye lens and eye globe are of oblate spheroidal shape.

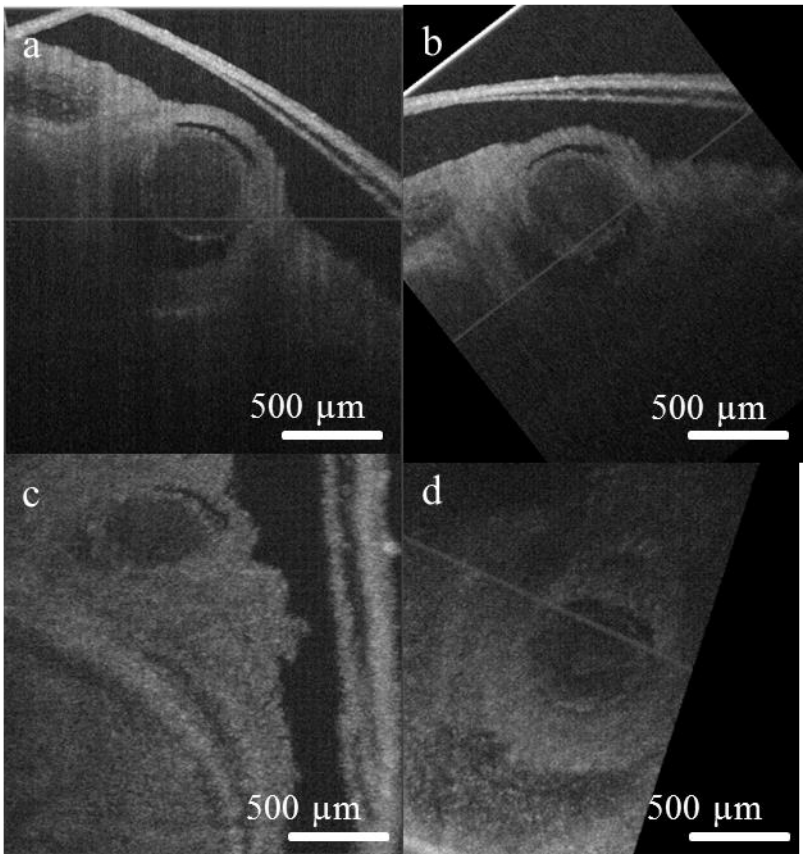

Figure 3.5. 2D cross-sectional OCT images before and after 3D rotation. (a) Axial cross-sectional image before 3D rotation. (b) Axial cross-sectional image after 3D rotation. (c) Transverse cross-sectional image before 3D rotation. (d) Transverse cross-sectional image after 3D rotation.

The major axis diameters from different stages of embryonic growth, obtained using OCT, are presented in Figure 3.7. It can be noted from Figures 3.7a and 3.7b (green bars) that there are roughly a 2-fold increase in major axis diameter of the eye lens and a 3-fold increase in major-axis diameter of the eye globe from E13.5 to E18.5. Using the measurements of the major and minor axes diameters, the volumes of the eye lens and the globe were computed using Equation (3.1). These results correlate well with Foster et al. [150], where the authors measured the major axis diameters and volumes of eye lens and globe using UBM (resolution of 40 µm). The results obtained using UBM (from [150]) are presented in Figure 4 (red bar). The major axis diameter measurements are within similar range, as compared to OCT measurements, across the different stages of

development. The values of standard deviation from the UBM measurements, however, are comparatively larger to the ones from OCT measurements, suggesting higher precision. The volume measurements are presented in Figure 3.8. It was determined that the volume of the eye lens and globe increased from 0.041±0.007 mm^3 to 0.46±0.03 mm^3 and from 0.07±0.01 mm^3 to 1.13±0.07 mm^3, respectively.

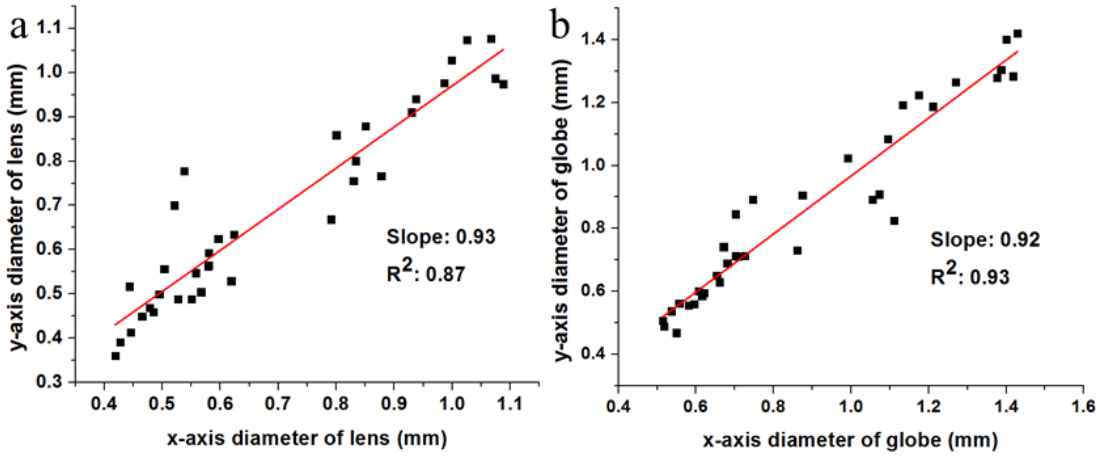

Figure 3.6. Plots of major axis diameter in x-axis and y-axis (transverse axes) of the eye (a) lens (b) globe.

3.6 Discussions

As evident from structural images of the embryo eyes, the contrast and resolution offered by OCT enable clear distinction of the embryonic ocular structures *in utero*. While the measurements of the major axis diameters of lens and globe using OCT between E13.5 to E18.5 are within similar range as the measurements from previous study using UBM [150], there are differences at individual stages between the two studies, such as the measurements of the major axes diameters of the eye lens from E16.5 to E18.5 and the measurements of the major axes diameters of the eye globe from E13.5 to E16.5. UBM has an inferior resolution (~40×60 μm) as compared to OCT (~12×15 μm). Moreover, the major and minor axis diameters were measured without any correction for the tilt of the eye. This can result in underestimating the actual diameters. It

can also be noted from [150], that the reported values for the volumes of the eye lens and the globe is not consistent with the respective values of the major axis diameters, as the authors likely used different equitation to obtain the final values.

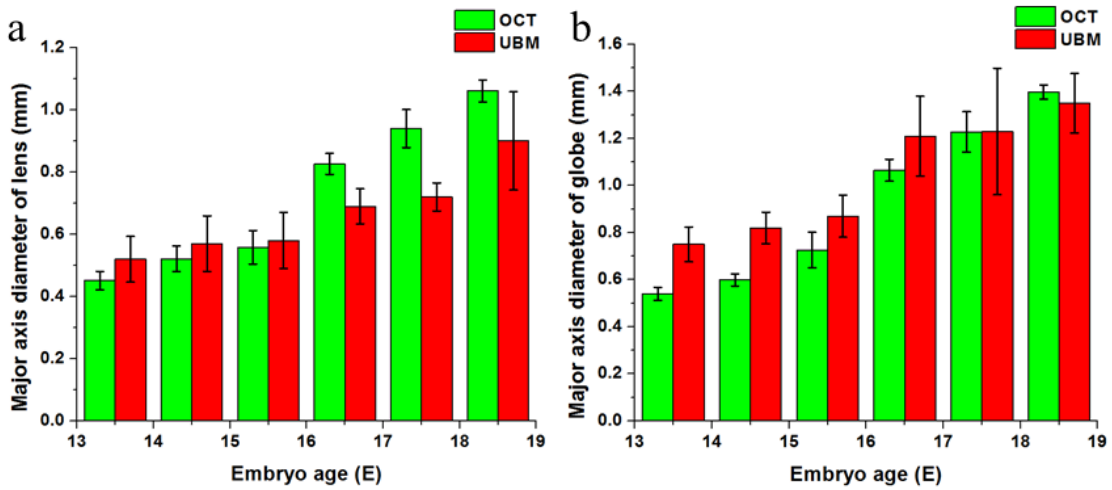

Figure 3.7. Major axis diameter measurements of the eye (a) lens (b) globe correlate well with previously reported UBM values. The UBM data is obtained from [150]. (n≥5)

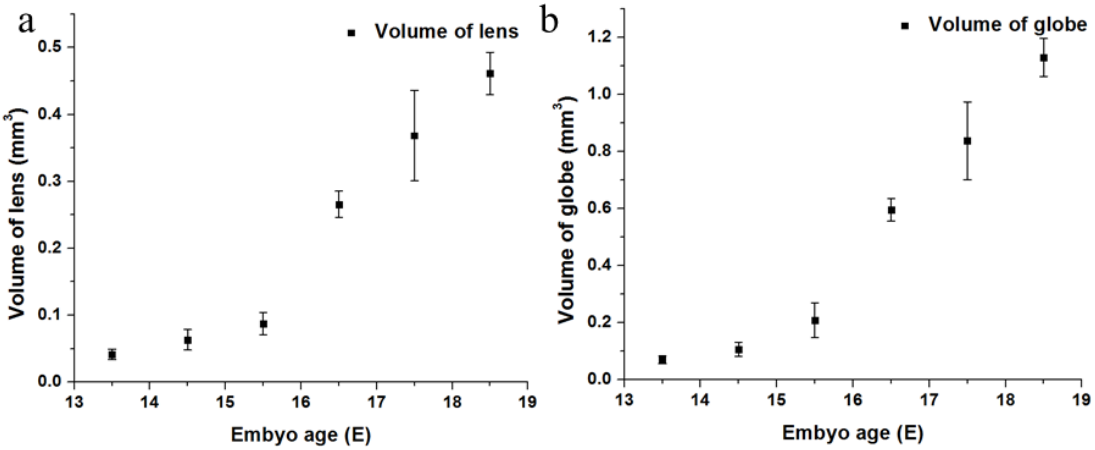

Figure 3.8. Plot of volume of the eye (a) lens (b) globe measured using OCT. (n≥5).

3.7 Conclusions

We have demonstrated that *in utero* OCT embryo imaging approach allows for live quantitative assessment of mouse embryonic ocular growth with higher resolution,

than other currently available methods. The volumes of the eye lens and the globe have been shown to increase from 0.041±0.007 mm^3 to 0.46±0.03 mm^3 and from 0.07±0.01 mm^3 to 1.13±0.07 mm^3, respectively, from E13.5 to E18.5. This study suggests that our approach can potentially be used for live quantitative characterization of ocular tissues in a variety of ocular research studies.

Chapter 4. Studying Effects of Alcohol Exposure on Brain Development in Mouse Fetus Using OCT

4.1 Introduction

The development of mammalian central nervous system (CNS) from the primitive neural tube till its matured form is comprised of a number of highly intricate processes. These processes include neuronal migration, axonal path finding, and myelination, amongst many others. Coordinated actions of thousands of genes guide the development of the CNS [154, 155]. The organization of the cerebral cortex occurs by appropriate positioning of the neuronal constituents into laminar and radial arrays which ultimately define their connectivity and function [156]. The migration of the cortical neurons from their origins to their final destinations occurs at precise schedule and well defined pathways [157, 158]. Several models have described the regionalization of the brain which occurs through several phases that transform the neural plate into highly refined regions [159, 160]. As the brain develops, the expressions of the genes become more region specific which leads to functional compartmentalization of the brain. Liscovitch et al., studied the changes in regional gene expressions of the mouse brain and compared it with human brain development [161].

The development of the brain is known to be affected by several genetic mutations. For example, the expansion of a CAG triplet repeat stretch within the coding region of the *Huntington* gene results in the mutant form of the protein which causes severe motor and cognitive impairment, brain atrophy and neuronal loss. This congenital condition is called Huntington's disease [162]. F52 is a protein which has multiple roles during the development of the brain particularly that of the cortex-related structures. Mice mutants which are F52-deficient have been associated with neural tube defects and

abnormal brain development [163]. Mutations in the gene (*FOXP2*) which codes for the Foxhead-box protein disrupt the neurite outgrowth during brain development in humans and other mammals [164]. This severely impacts the cognitive function in humans resulting in monogenic speech and language disorders. A study using knockout mouse model for hypoxia-inducible factor 1α (HIF-1α) determined that apoptosis of neural cells occur due to vascular regression in the telencephalon which results in reduction of neural cells and impairment of spatial memory [165].

Other than genetic causes, exposure to environmental agents such as drugs and alcohol are also known to hamper normal brain development. Drugs such as cocaine have previously shown to cause severe detrimental effects during brain development [166-168]. Prenatal exposure to nicotine can cause several long term effects on the offspring such as impaired fertility, type 2 diabetes and obesity [169]. Nicotine has also been shown to affect critical neural pathways during brain development [170]. Consumption of caffeine during pregnancy can also increase the chances of affecting the development of CNS in the offspring [171]. Exposure to ionizing radiation and even ultrasound waves has been demonstrated to affect normal development of the brain in rodents [172, 173].

Maternal consumption of alcohol during pregnancy is the leading non-genetic cause of mental retardation in children in the United States, and can lead to a cluster of permanent physical and mental defects in fetuses that are collectively termed the Fetal Alcohol Spectrum Disorder (FASD). It is estimated that 2-5% of children in the United States suffer from alcohol related birth defects [174]. Children suffering from FASD are characterized by growth deficiency, disorders in the CNS and distinct facial patterns. Previous research has shown that ethanol can directly affect various aspects of brain

development in the fetus. Camarillo et al., determined that ethanol is responsible for activation of genes which are related to cell migration and can influence the maturation of neural stem and progenitor cells [175]. Exposure to alcohol can induce apoptosis in neural crest cells and oligodendrocytes in a developing fetus [176, 177]. Alcohol-exposed pregnant mice have previously been used to study the emergence of FASD during fetal development [178, 179].

4.2 Imaging modalities for studying brain development

Histology based methods have been used for monitoring the developmental process in embryos traditionally [158, 180, 181]. Histology based methods have provided valuable information regarding anatomical structures in the past; however, these methods require destruction of the specimen making live imaging impossible. These techniques cannot provide 3D information, prone to tissue processing and sectioning artifacts, and they are also time consuming and inefficient.

Magnetic resonance imaging (MRI) is a noninvasive imaging modality capable of 3D imaging, which has been used extensively for *in vivo* phenotype analysis for wide variety of adult mouse models for neurological diseases [182, 183]. Although conventional MRI provides sufficient contrast using relaxation-based (T_1, T_2) mechanisms in adult mice where myelin is abundant, it poses a challenge in imaging developing brain in neonates and fetuses brain structures are unmyelinated. Enhanced tissue differentiation in the developing mouse brain can be achieved by using Magnetic Resonance Micro-histology with Mn-DPDP and Gd-DTPA as contrast agents [184]. Contrast enhanced forms of the conventional MRI, such as diffusion tensor imaging (DTI) [185, 186] and Manganese-enhanced MRI (MEMRI) [187] have been found to

useful in imaging developing brain in neonates. DTI has not yet been demonstrated *in vitro* conditions. MEMRI has been shown to be capable to perform longitudinal studies such as analysis of delayed brain damage due to hypoxic-ischemic injury in neonatal rats [188]. MEMRI has also been shown to perform *in utero* imaging of central nervous system in wild-type and *Nkx2.1* mutant mouse embryos. This system could achieve a resolution of 100 µm and provided sufficient contrast for volumetric analysis of CNS structures. However, the study demonstrated that the embryos were susceptible to Mn-induced lethality thereby making this method incompatible to perform longitudinal studies [189].

Ultrasound biomicroscopy (UBM) is real-time imaging modality which has been well established to perform *in utero* imaging of mouse embryos at near optical resolution. One of the earliest uses of UBM for *in utero* imaging of mouse embryos was to analyze the embryonic brain development with a resolution of 50 µm at ~10 frame rate per second (fps). This study could record deletion of midhindbrain which is associated with null mutation of *Wnt-1* gene [147]. Current commercially available UBM systems can achieve ~100 fps with spatial resolution of 30 µm axial and 70 µm transverse resolutions and can image up to 10 mm in depth [190]. UBM has also been applied for *in utero* manipulations of mouse embryos [191, 192]. One of the main limitations of UBM is poor contrast compared to optical imaging systems. Previous studies have also suggested that prenatal exposure to ultrasound can also have hazardous consequences [173, 193].

Optical coherence tomography (OCT) is a noninvasive imaging modality which is capable of 3D and real-time imaging, offers high optical contrast and does not require any external contrast agents [1]. High imaging resolution (in the µm range) and depth

penetration of a few millimeters in tissue makes OCT an attractive tool to study the development of fetal mice. Recently, our group demonstrated the capacity of SSOCT to be adapted to longitudinal studies in mice embryos, to monitor development of morphological features such as the brain, limbs and ocular structures, *in utero* [62, 153]. In this study, SSOCT and high-resolution ultrasound imaging were used to compare the volumes of lateral ventricles between control fetal mice and fetal mice exposed to ethanol *in utero*, during the second trimester-equivalent period of pregnancy, a critical period for neurogenesis in the developing brain [194].

4.3 Experimental setup

4.3.1 Animal model

All procedures were performed in accordance with approved IACUC protocols. Timed-Pregnant mice (C57Bl6, Harlan Laboratories, Houston, TX) were housed in an AALAC-accredited animal facility at Texas A&M Health Science Center. On gestational day 12.5, pregnant mice were divided into a control and an ethanol-exposed group. Ethanol-exposed pregnant females received a binge-like bolus of ethanol (3 g/kg b.wt) by intragastric gavage, twice daily, between GD12.5 and GD14.5, to model ethanol exposure during the second-trimester equivalent period of neurogenesis, whereas control animal received water by gavage at the same time intervals. Previous research showed that intragastric gavage with this dose of ethanol resulted in a mean peak maternal blood ethanol concentrations of 117 mg/dl [179], representing a level of binge-like intoxication readily achieved in non-alcoholic human populations. Two hours following the final exposure period, pregnant dams were over-anesthetized with Ketamine and Xylazine and euthanized by cervical dislocation. Ethanol-exposed and control fetuses were dissected

out of the uterine horns and fixed in 4% paraformaldehyde overnight and transferred to PBS for imaging. Five fetuses from 2 mothers were used each for ethanol-exposed and control experiments. Following the imaging procedures, fetuses were embedded in paraffin and serial sections obtained. Every 10^{th} section was stained with Hematoxylin and Eosin, and the brain visualized by light microscopy.

4.3.2 Brain imaging

Paraformaldehyde fixed fetuses were initially imaged using a high resolution Vevo 2100 ultrasound imaging system, coupled to a MS550D Microscan^{TM} transducer on a motorized stage, with a center frequency of 40MHz (Visualsonics, Canada). Image slices were acquired in B-mode, through the fetal head with a 0.032 mm step size. The same fetuses were then subjected to SSOCT imaging, for volumetric analysis and quantification of fetal mouse brains. The SSOCT system comprises of a broadband laser source (Thorlabs, SL1325-P16), which has a central wavelength of 1325 nm, bandwidth of 100 nm, output power of 12 mW and A-line rate of 16 kHz. The axial and transverse resolutions of the system are 12 and 15 μm, respectively (in air). Each 3-D volume contained 512×512 A-lines.

4.4 Data processing and analysis

4.4.1 GUI for manual tracing of brain ventricles

Both the ultrasound imaging and the SSOCT systems contain 3D information of the lateral ventricles in the brain of the fetuses used in the study. A MATLAB based GUI was created to assist in manual segmentation of the lateral ventricles of the fetuses. The front end of the GUI is displayed in Figure 4.1.

The GUI can import 3D images in '.IMG', '.JPG' or '.TIFF' formats. The GUI displays one single 2D cross-section at a particular instant and by using the slider, different 2D cross-sections can be viewed. The manual tracing is enabled by clicking in the 'Start Drawing' button and performed by left-clicking the mouse and move along the edges of the ventricles. The coordinates over which the cursor is moving is recorded during the tracing process. The tracing is completed by releasing the mouse and the trace is completed by joining the first and the last points creating a closed figure. The red line in Figure 4.1 depicts the manual tracing of the left ventricle at a particular 2D cross-section. If the tracing is incorrect, it can be redrawn by pressing the 'Undo' button and restarting the tracing process. The number of pixels enclosed in the closed figure is then computed using the 'polyarea' function available in MATLAB. The choice of 'Left Ventricle' or 'Right Ventricle' can be chosen by selecting the corresponding radio button. The number of pixels enclosed in the ventricles can then be saved onto a MS Excel sheet for further computations.

Figure 4.1. MATLAB based GUI for manual segmentation of the lateral ventricles.

4.4.2 Computing the volume of lateral ventricles

To compute the volume of the lateral ventricles, the number of pixels enclosed in individual 2D cross-section is computed for both the left and right ventricles and repeating it for all the 2D cross-sections which contain the ventricles. The volume is computed by multiplying the total number of pixels enclosed in all the cross-sections with the volume of a voxel.

4.4.3 Statistical analysis

The average volume of lateral ventricles from the control and the ethanol-exposed groups were used for statistical analysis. Each group had 5 fetuses. A two-sample Kolmogorov–Smirnov test was then performed to determine the statistical significance of the difference between ethanol-treated and control groups. Finally, Pearson's correlation coefficients (r) were computed to determine the extent to which variance in SSOCT measurements were predictive of variance in ultrasound measurements.

4.5 Results

To compare the quality of images obtained using SSOCT and ultrasound (US) systems, 2D transverse images containing the lateral ventricles from a control fetus is depicted in Figure 4.2. It can be observed from the figure that SSOCT system (Figure 4.2a) provides better resolution and contrast compared to the US imaging system (Figure 4.2b). The boundaries of the lateral ventricles are much more distinct in the OCT image compared to the US image, enabling more accurate segmentation of the ventricles. Regions such as the ventricular zone (VZ) and the cortical plate (CP) can clearly be distinguished from the OCT image, whereas, the US system does not provide sufficient

contrast between the two regions. These results clearly suggest the advantage of using OCT over US for analyzing morphological structures in brain of mouse fetuses.

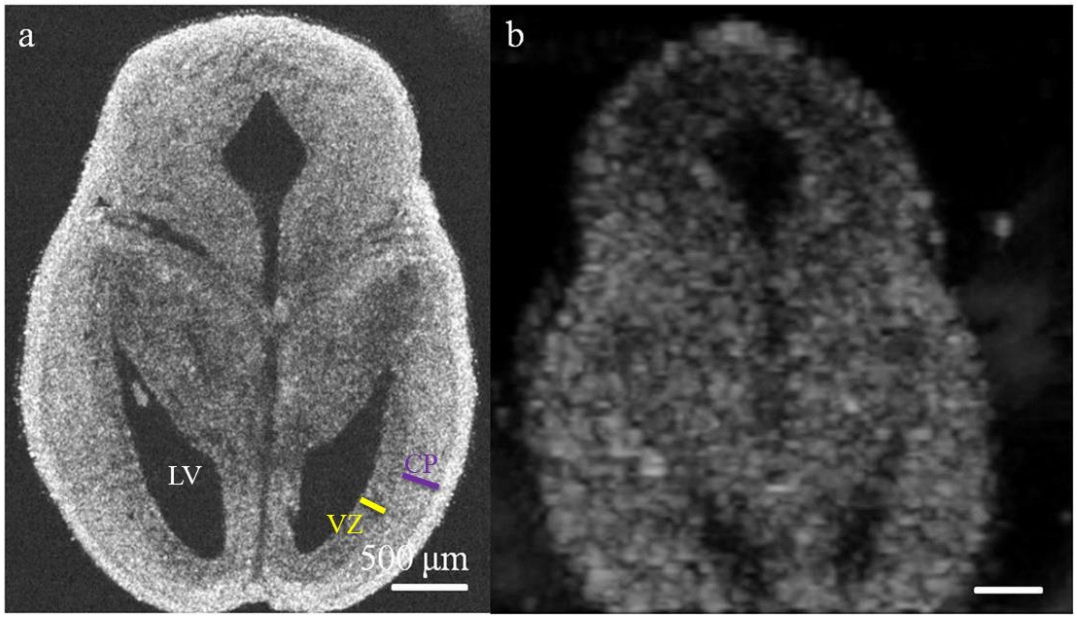

Figure 4.2. Comparison between images obtained using OCT and ultrasound imaging. 2D cross-sectional images obtained using (a) OCT (b) ultrasound imaging. Scale bar, 500µm. LV – Lateral ventricles, VZ – Ventricular zone, CP – Cortical plate. [195].

Typical 2D transverse cross-sectional images for control and ethanol-exposed fetuses, obtained using SSOCT, are presented in Figure 4.3a and 4.3b, respectively. It can be clearly observed that the ventricular regions are discernible and are dilated in the ethanol-exposed fetus compared to the control. The number of pixels enclosed within the lateral ventricles in a single 2D transverse cross-section was determined using the MATLAB based GUI. The total number of pixels encompassing the entire 3D lateral ventricular region was measured from individual 2D images and multiplied by the voxel volume to obtain the total volume. The volumes of the right and left ventricles were then averaged for individual fetuses. The statistical measurement from 5 samples, each from control and ethanol-exposed fetuses is presented in Figure 4.4. The averaged volume of lateral ventricles was measured to be 0.18±0.07 mm^3 for control and 0.38±0.18 mm^3 for

ethanol-exposed fetuses. To verify the measurements made with OCT, high-resolution ultrasound (US) was also was also used to obtain 3D images of the same set of fetuses and the ventricular volume was measured using the same method. Typical 2D transverse cross-sectional images for control and ethanol-exposed fetuses, obtained using US, are presented in Figure 4.3c and 4.3d, respectively. The averaged lateral ventricular volumes of control and ethanol-exposed fetuses were measured to be 0.19±0.14 mm^3 and 0.33±0.16 mm^3, respectively (Figure 4.4).

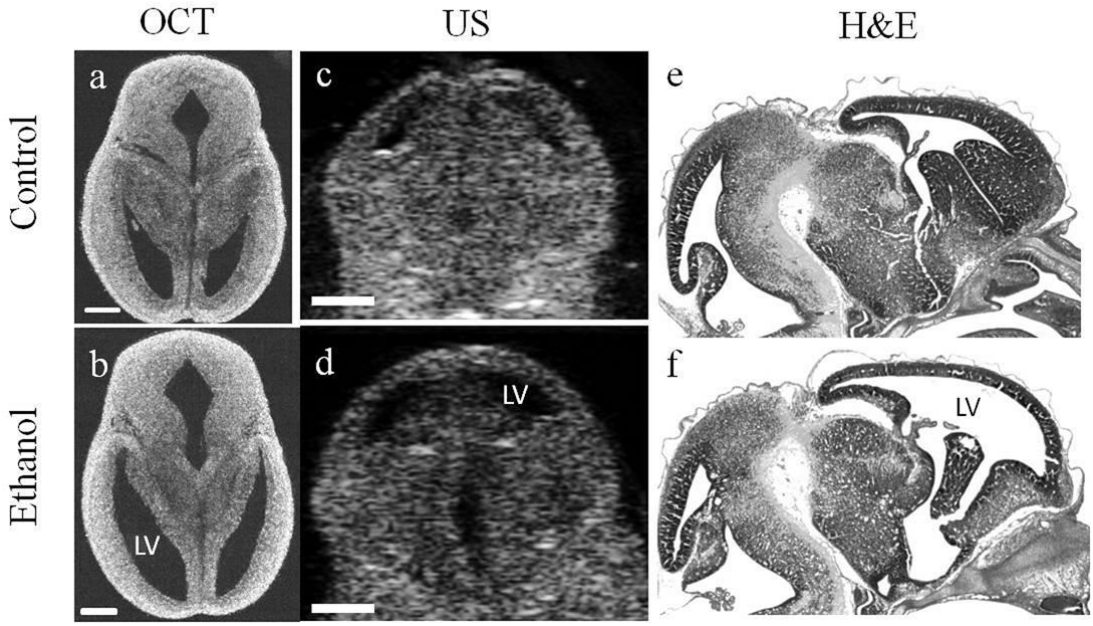

Figure 4.3. Effect of ethanol on mouse fetal brain development at GD14.5. (a,b) OCT images in horizontal section (c,d) US images in the coronal plane (e,f) H&E images in sagittal section of fetal brains from both control and ethanol treated pregnant dams. Scale bar, 500μm. [195].

The measurements from OCT are within the same range of the measurements obtained with ultrasound imaging. Moreover, there was an overall statistically significant correlation between ventricular volume estimates obtained by OCT and ultrasound imaging (Pearson's $r = 0.633$, $p<0.005$). However, ventricular margins were not as clearly defined in the ultrasound-derived compared to OCT-derived images because of the lower contrast and resolution (~30 μm) of these images, and consequently, resulted in

a 2-fold increase in the variance estimate of the ventricular volume in control fetuses compared to SSOCT imaging. The results (Figure 4.4) from *ex vivo* ultrasound imaging alone suggest that there is no statistical difference between the lateral ventricle volumes from control and ethanol-exposed fetuses (two sample Kolmogorov–Smirnov test, $p>0.05$).

4.6 Discussions

Ventricular defects of the brain are common symptoms of defective neurodevelopment [196], caused by a variety of agents including fetal alcohol exposure [197]. High-resolution imaging and early accurate assessment of ventricular volume may facilitate the conduct of pre-clinical interventional studies and the testing of novel therapeutic approaches for ameliorating *in utero* damage. The challenge in measuring the volume of ventricles with high accuracy, involves the segmentation of ventricular regions in consecutive 2D images with high precision. This study demonstrates that OCT offers superior resolution and contrast compared to US imaging which enables higher accuracy during segmentation of the ventricles (Figure 4.2).

This study demonstrates that the average volume of lateral ventricles is twice as higher for the ethanol-exposed group compared to the control group (Figure 4.4). Interestingly, the standard deviation for the observed ventricular volume was also larger for the group of ethanol-exposed fetuses compared to the control group. This increased variance in ventricular volume reflects variation in susceptibility of individual fetuses to the teratogenic effects of ethanol, an observation that has been made in human populations as well [198]. Even though OCT has superior resolution and contrast, however, unlike ultrasound imaging, it has limited imaging depth due to light attenuation

in tissues. Nevertheless, our group has recently demonstrated possibility of *in utero* imaging of mice embryonic organs, including brain [62].

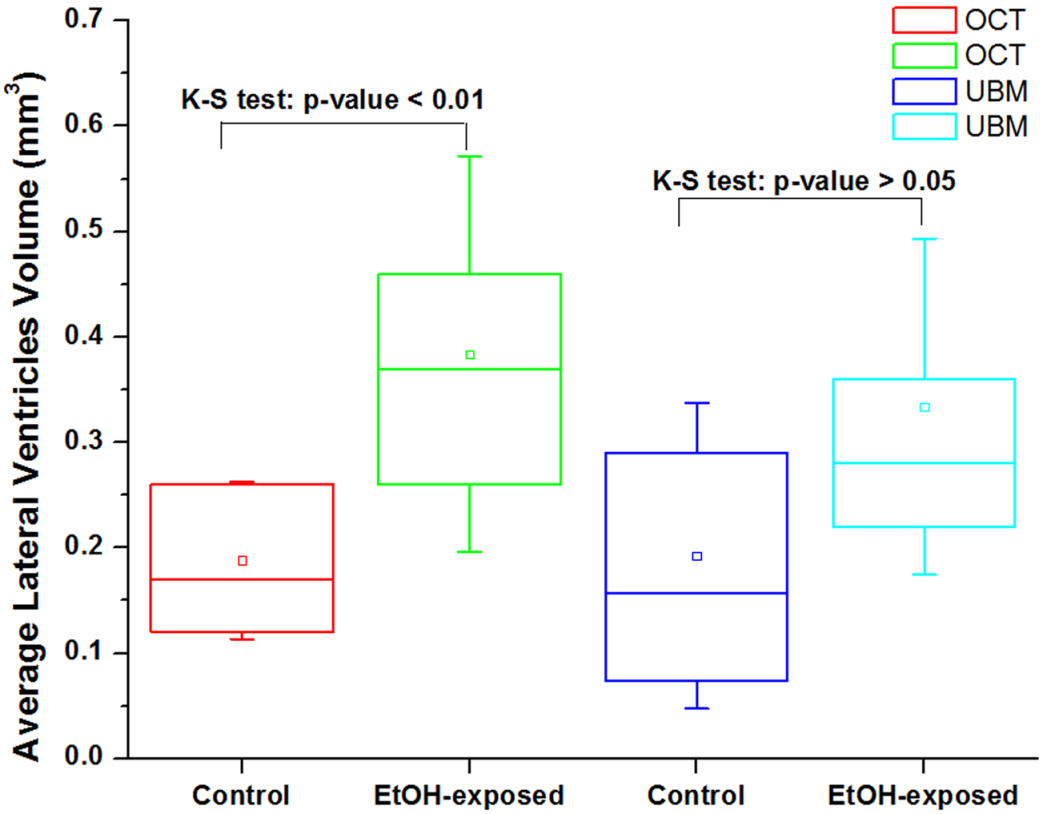

Figure 4.4. Measurements of lateral ventricles of control and ethanol-exposed fetuses at GD14.5 obtained from SSOCT and US images; The whiskers represent Standard Deviation, and small hollow squares represent the mean of the data distribution. [195].

4.7 Conclusions

Maternal alcohol consumption during pregnancy is a well-established cause of fetal growth retardation, and the dilation of lateral ventricles is an important index of decreased brain growth. Our data suggest that binge-like episodes of ethanol exposure during the second trimester-equivalent period of neurogenesis, at levels below those attained in alcoholic populations, nevertheless result in a two-fold, statistically significant dilation of the lateral ventricles of the fetal brain. Moreover, OCT is more accurate than *ex vivo* ultrasound imaging, and is a useful and sensitive imaging modality for preclinical,

whole animal studies, to assess the effects of drugs of abuse and perhaps other environmental teratogens on fetal growth and development. It will be important in future studies to identify the range of quantitative OCT-derived measurements that can serve as useful biomarkers for fetal teratogenesis.

Chapter 5. Conclusions

5.1 Summary

This dissertation focuses on the potential use of optical coherence tomography (OCT) to monitor morphological features during mouse embryonic development. OCT offers high imaging resolution (~ 10 μm) in both axial and transverse directions, a high optical contrast without the requirement of external contrast agents, and a sufficiently high penetration depth (~ 1-2 mm), which are ideal characteristics for qualitative and quantitative monitoring of mouse embryonic development.

Chapter 2 focuses on potential use of OCT for early diagnosis of congenital cardiovascular diseases (CVD) in a mouse embryo model. Significant changes in the embryonic and extra-embryonic vasculature occur during the mouse embryo at E8.5 to E9.5. An abnormal development and remodeling of the vasculature during these stages suggest CVD. Blood vasculature has been imaged by implementing Doppler OCT (DOCT) and speckle variance (SV) algorithms and a comparative analysis was performed. The advantages of using SVOCT over Doppler OCT were demonstrated for 3D flow detection using a milk flow model. Detection of 3D vasculature in the yolk sac of E8.5 and E9.5 embryos was demonstrated. Comparisons between DOCT and SV imaging for 3D reconstruction of vasculature reveal that, although both techniques perform equally well in vessels have high axial flow component; SV imaging is better able to detect the vasculature in the yolk sac where flow is perpendicular. The results demonstrate SV imaging as an efficient tool for early diagnosis for congenital CVD.

The ability of OCT for monitoring ocular development in mouse embryos *in utero* conditions was explored in Chapter 3. Volume measurements of the eye lens and the eye

globe was used to monitor ocular development. The volumes of the eye lens and the globe have been shown to increase from 0.041±0.007 mm^3 to 0.46±0.03 mm^3 and from 0.07±0.01 mm^3 to 1.13±0.07 mm^3, respectively, from E13.5 to E18.5.

The advantage of using OCT over high-resolution ultrasound (US) to study effects of prenatal exposure to alcohol on the development of brain was demonstrated in Chapter 4. Both OCT and US were used to quantify the volume of the lateral ventricles of the brain in ethanol-exposed and control fetuses. The averaged volume of lateral ventricles was measured to be 0.18±0.07 mm^3 for control and 0.38±0.18 mm^3 for ethanol-exposed fetuses using OCT. The averaged lateral ventricular volumes of control and ethanol-exposed fetuses were measured to be 0.19±0.14 mm^3 and 0.33±0.16 mm^3, respectively, using US. The ventricular margins were not as clearly defined in the US images compared to OCT images, due to lower contrast and resolution (~30 μm) of these images, and consequently, resulted in a 2-fold increase in the variance estimate of the ventricular volume in control fetuses compared to OCT imaging.

5.2 Conclusions

This dissertation demonstrated that:

1) SVOCT has clear advantages to detect 3D vasculature compared to Doppler OCT. OCT is a potential tool for diagnosis of CVD in mouse embryos.
2) OCT can be potentially used to perform longitudinal studies on ocular development of mouse embryos.
3) OCT is superior to US imaging for monitoring brain development in mouse fetuses. OCT-derived measurements can potentially serve as useful biomarkers for fetal teratogenesis.

References

[1] D. Huang, E. A. Swanson, C. Lin, J. S. Schuman, W. G. Stinson, W. Chang, M. R. Hee, T. Flotte, K. Gregory, and C. A. Puliafito, "Optical Coherence Tomography," *Science,* vol. 254, pp. 1178-1181, November 22, 1991 1991.

[2] P. H. Tomlins and R. K. Wang, "Theory, Developments and Applications of Optical Coherence Tomography," *J Phys D Appl Phys,* vol. 38, p. 2519, 2005.

[3] W. Drexler and J. G. Fujimoto, *Optical Coherence Tomography : Technology and Applications*. New York: Springer, 2008.

[4] A. F. Fercher, W. Drexler, C. K. Hitzenberger, and T. Lasser, "Optical Coherence Tomography - Principles and Applications," *Reports on Progress in Physics,* vol. 66, p. 239, 2003.

[5] T. Gambichler, G. Moussa, M. Sand, D. Sand, P. Altmeyer, and K. Hoffmann, "Applications of Optical Coherence Tomography in Dermatology," *J Dermatol Sci,* vol. 40, pp. 85-94, Nov 2005.

[6] B. Colston, U. Sathyam, L. Dasilva, M. Everett, P. Stroeve, and L. Otis, "Dental Oct," *Optics Express,* vol. 3, pp. 230-8, Sep 1998.

[7] X. D. Li, S. A. Boppart, J. Van Dam, H. Mashimo, M. Mutinga, W. Drexler, M. Klein, C. Pitris, M. L. Krinsky, M. E. Brezinski, and J. G. Fujimoto, "Optical Coherence Tomography: Advanced Technology for the Endoscopic Imaging of Barrett's Esophagus," *Endoscopy,* vol. 32, pp. 921-30, Dec 2000.

[8] Y. Yang, A. Dubios, X. P. Qin, and R. K. Wang, "Investigation of Optical Coherence Tomography as an Imaging Modality Intissue Engineering," *Physics in Medicine and Biology,* vol. 51, p. 1649, 2006.

[9] Z. Chen, T. E. Milner, S. Srinivas, X. Wang, A. Malekafzali, M. J. C. van Gemert, and J. S. Nelson, "Noninvasive Imaging of in Vivo Blood Flow Velocity Using Optical Doppler Tomography," *Optics Letters,* vol. 22, pp. 1119-1121, Jul 1997.

[10] J. A. Izatt, M. D. Kulkarni, S. Yazdanfar, J. K. Barton, and A. J. Welch, "In Vivo Bidirectional Color Doppler Flow Imaging of Picoliter Blood Volumes Using Optical Coherence Tomography," *Optics Letters,* vol. 22, pp. 1439-1441, Sep 1997.

[11] W. Drexler and J. Fujimoto, *Optical Coherence Tomography: Technology and Applications*. Berlin: Springer, 2008.

[12] G. J. Tearney, B. E. Bouma, and J. G. Fujimoto, "High-Speed Phase- and Group-Delay Scanning with a Grating-Based Phase Control Delay Line," *Optics Letters,* vol. 22, pp. 1811-1813, Dec 1997.

[13] S. Yun, G. Tearney, B. Bouma, B. Park, and J. de Boer, "High-Speed Spectral-Domain Optical Coherence Tomography at 1.3 Mum Wavelength," *Opt Express,* vol. 11, pp. 3598-604, Dec 29 2003.

[14] Z. Hu and A. M. Rollins, "Fourier Domain Optical Coherence Tomography with a Linear-in-Wavenumber Spectrometer," *Opt. Lett.,* vol. 32, pp. 3525-3527, 2007.

[15] S. R. Chinn, E. A. Swanson, and J. G. Fujimoto, "Optical Coherence Tomography Using a Frequency-Tunable Optical Source," *Optics Letters,* vol. 22, pp. 340-342, Mar 1997.

[16] T.-J. Ahn and D. Y. Kim, "Analysis of Nonlinear Frequency Sweep in High-Speed Tunable Laser Sources Using a Self-Homodyne Measurement and Hilbert Transformation," *Applied Optics,* vol. 46, pp. 2394-2400, Apr 2007.

[17] R. K. Manapuram, V. G. R. Manne, and K. V. Larin, "Development of Phase-Stabilized Swept-Source Oct for the Ultrasensitive Quantification of Microbubbles," *Laser Physics,* vol. 18, pp. 1080-1086, 2008/09/01 2008.

[18] C. M. Eigenwillig, B. R. Biedermann, G. Palte, and R. Huber, "K-Space Linear Fourier Domain Mode Locked Laser and Applications for Optical Coherence Tomography," *Optics Express,* vol. 16, pp. 8916-8937, Jun 2008.

[19] M. Wojtkowski, V. Srinivasan, T. Ko, J. Fujimoto, A. Kowalczyk, and J. Duker, "Ultrahigh-Resolution, High-Speed, Fourier Domain Optical Coherence Tomography and Methods for Dispersion Compensation," *Optics Express,* vol. 12, pp. 2404-2422, May 2004.

[20] B. Potsaid, I. Gorczynska, V. J. Srinivasan, Y. Chen, J. Jiang, A. Cable, and J. G. Fujimoto, "Ultrahigh Speed Spectral / Fourierdomain Oct Ophthalmic Imaging At70,000 to 312,500 Axial Scans Per Second," *Optics Express,* vol. 16, pp. 15149-15169, Sep 2008.

[21] W. Wieser, B. R. Biedermann, T. Klein, C. M. Eigenwillig, and R. Huber, "Multi-Megahertz Oct: High Quality 3d Imaging at 20 Million a-Scans and 4.5 Gvoxels Per Second," *Optics Express,* vol. 18, pp. 14685-14704, Jul 5 2010.

[22] R. Leitgeb, C. Hitzenberger, and A. Fercher, "Performance of Fourier Domain Vs. Time Domain Optical Coherence Tomography," *Optics Express,* vol. 11, pp. 889-894, Apr 2003.

[23] M. Choma, M. Sarunic, C. Yang, and J. Izatt, "Sensitivity Advantage of Swept Source and Fourier Domain Optical Coherence Tomography," *Optics Express,* vol. 11, pp. 2183-2189, Sep 2003.

[24] J. F. de Boer, B. Cense, B. H. Park, M. C. Pierce, G. J. Tearney, and B. E. Bouma, "Improved Signal-to-Noise Ratio in Spectral-Domain Compared with Time-Domain Optical Coherence Tomography," *Optics Letters,* vol. 28, pp. 2067-2069, Nov 2003.

[25] Z. Yaqoob, J. Wu, and C. Yang, "Spectral Domain Optical Coherence Tomography: A Better Oct Imaging Strategy," *Biotechniques,* vol. 39, pp. S6-13, Dec 2005.

[26] J. M. Schmitt, S. H. Xiang, and K. M. Yung, "Speckle in Optical Coherence Tomography," *J Biomed Opt,* vol. 4, pp. 95-105, Jan 1999.

[27] B. F. Kennedy, T. R. Hillman, A. Curatolo, and D. D. Sampson, "Speckle Reduction in Optical Coherence Tomography by Strain Compounding," *Optics Letters,* vol. 35, pp. 2445-2447, Jul 15 2010.

[28] D. L. Marks, T. S. Ralston, and S. A. Boppart, "Speckle Reduction by I-Divergence Regularization in Optical Coherence Tomography," *Journal of the Optical Society of America a-Optics Image Science and Vision,* vol. 22, pp. 2366-2371, Oct 2005.

[29] D. C. Adler, T. H. Ko, and J. G. Fujimoto, "Speckle Reduction in Optical Coherence Tomography Images by Use of a Spatially Adaptive Wavelet Filter," *Optics Letters,* vol. 29, pp. 2878-2880, Dec 15 2004.

[30] M. Pircher, E. Gotzinger, R. Leitgeb, A. F. Fercher, and C. K. Hitzenberger, "Speckle Reduction in Optical Coherence Tomography by Frequency Compounding," *Journal of Biomedical Optics,* vol. 8, pp. 565-569, Jul 2003.

[31] N. Iftimia, B. E. Bouma, and G. J. Tearney, "Speckle Reduction in Optical Coherence Tomography by "Path Length Encoded" Angular Compounding," *Journal of Biomedical Optics,* vol. 8, pp. 260-263, Apr 2003.

[32] K. W. Gossage, T. S. Tkaczyk, J. J. Rodriguez, and J. K. Barton, "Texture Analysis of Optical Coherence Tomography Images: Feasibility for Tissue Classification," *Journal of Biomedical Optics,* vol. 8, pp. 570-5, Jul 2003.

[33] D. A. Zimnyakov, V. V. Tuchin, and A. A. Mishin, "Spatial Speckle Correlometry in Applications to Tissue Structure Monitoring," *Applied Optics,* vol. 36, pp. 5594-607, Aug 1997.

[34] C. Kasai, K. Namekawa, A. Koyano, and R. Omoto, "Real-Time Two-Dimensional Blood Flow Imaging Using an Autocorrelation Technique," *Sonics and Ultrasonics, IEEE Transactions on,* vol. 32, pp. 458-464, 1985.

[35] A. Mariampillai, B. A. Standish, N. R. Munce, C. Randall, G. Liu, J. Y. Jiang, A. E. Cable, I. A. Vitkin, and V. X. D. Yang, "Doppler Optical Cardiogram Gated 2d Color Flow Imaging at 1000 Fps and 4d in Vivo Visualization of Embryonic Heart at 45 Fps on a Swept Source Oct System," *Optics Express,* vol. 15, pp. 1627-1638, Feb 2007.

[36] B. Vakoc, S. Yun, J. de Boer, G. Tearney, and B. Bouma, "Phase-Resolved Optical Frequency Domain Imaging," *Optics Express,* vol. 13, pp. 5483-5493, Jul 2005.

[37] R. K. Wang, S. L. Jacques, Z. Ma, S. Hurst, S. R. Hanson, and A. Gruber, "Three Dimensional Optical Angiography," *Opt. Express,* vol. 15, pp. 4083-4097, April 2007 2007.

[38] R. K. Wang, "Directional Blood Flow Imaging in Volumetric Optical Microangiography Achieved by Digital Frequency Modulation," *Optics Letters,* vol. 33, pp. 1878-80, Aug 2008.

[39] R. K. Wang and L. An, "Doppler Optical Micro-Angiography for Volumetric Imaging of Vascular Perfusion in Vivo," *Optics Express,* vol. 17, pp. 8926-40, May 2009.

[40] Y. Jia and R. K. Wang, "Optical Micro-Angiography Images Structural and Functional Cerebral Blood Perfusion in Mice with Cranium Left Intact," *Journal of Biophotonics,* Feb 2010.

[41] J. Fingler, D. Schwartz, C. Yang, and S. E. Fraser, "Mobility and Transverse Flow Visualization Using Phase Variance Contrast with Spectral Domain Optical Coherence Tomography," *Opt. Express,* vol. 15, pp. 12636-12653, 2007.

[42] A. Mariampillai, M. K. K. Leung, M. Jarvi, B. A. Standish, K. Lee, B. C. Wilson, A. Vitkin, and V. X. D. Yang, "Optimized Speckle Variance Oct Imaging of Microvasculature," *Optics Letters,* vol. 35, pp. 1257-1259, Apr 15 2010.

[43] A. Mariampillai, B. A. Standish, E. H. Moriyama, M. Khurana, N. R. Munce, M. K. K. Leung, J. Jiang, A. Cable, B. C. Wilson, I. A. Vitkin, and V. X. D. Yang, "Speckle Variance Detection of Microvasculature Using Swept-Source Optical Coherence Tomography," *Opt. Lett.,* vol. 33, pp. 1530-1532, June 2008 2008.

[44] Y. Wang and R. K. Wang, "Autocorrelation Optical Coherence Tomography for Mapping Transverse Particle-Flow Velocity," *Optics Letters,* vol. 35, pp. 3538-3540, Nov 1 2010.

[45] X. Liu, Y. Huang, J. C. Ramella-Roman, S. A. Mathews, and J. U. Kang, "Quantitative Transverse Flow Measurement Using Optical Coherence Tomography Speckle Decorrelation Analysis," *Optics Letters,* vol. 38, pp. 805-807, Mar 1 2013.

[46] J. Barton and S. Stromski, "Flow Measurement without Phase Information in Optical Coherence Tomography Images," *Opt. Express,* vol. 13, pp. 5234-5239, 2005.

[47] T. Glaser, L. Jepeal, J. G. Edwards, S. R. Young, J. Favor, and R. L. Maas, "Pax6 Gene Dosage Effect in a Family with Congenital Cataracts, Aniridia, Anophthalmia and Central-Nervous-System Defects," *Nature Genetics,* vol. 8, pp. 203-203, Oct 1994.

[48] K. B. Avraham, T. Hasson, K. P. Steel, D. M. Kingsley, L. B. Russell, M. S. Mooseker, N. G. Copeland, and N. A. Jenkins, "The Mouse Snell's Waltzer Deafness Gene Encodes an Unconventional Myosin Required for Structural Integrity of Inner Ear Hair Cells," *Nat Genet,* vol. 11, pp. 369-75, Dec 1995.

[49] P. Dolle, A. Dierich, M. LeMeur, T. Schimmang, B. Schuhbaur, P. Chambon, and D. Duboule, "Disruption of the Hoxd-13 Gene Induces Localized Heterochrony Leading to Mice with Neotenic Limbs," *Cell,* vol. 75, pp. 431-41, Nov 5 1993.

[50] F. M. LaFerla, B. T. Tinkle, C. J. Bieberich, C. C. Haudenschild, and G. Jay, "The Alzheimer's a Beta Peptide Induces Neurodegeneration and Apoptotic Cell Death in Transgenic Mice," *Nat Genet,* vol. 9, pp. 21-30, Jan 1995.

[51] G. A. Cox, Y. Sunada, K. P. Campbell, and J. S. Chamberlain, "Dp71 Can Restore the Dystrophin-Associated Glycoprotein Complex in Muscle but Fails to Prevent Dystrophy," *Nature Genetics,* vol. 8, pp. 333-339, Dec 1994.

[52] E. A. Lindsay, A. Botta, V. Jurecic, S. Carattini-Rivera, Y. C. Cheah, H. M. Rosenblatt, A. Bradley, and A. Baldini, "Congenital Heart Disease in Mice Deficient for the Digeorge Syndrome Region," *Nature,* vol. 401, pp. 379-83, Sep 23 1999.

[53] S. A. Boppart, M. E. Brezinski, B. E. Bouma, G. J. Tearney, and J. G. Fujimoto, "Investigation of Developing Embryonic Morphology Using Optical Coherence Tomography," *Developmental Biology,* vol. 177, pp. 54-63, Jul 1996.

[54] L. Kagemann, H. Ishikawa, J. Zou, P. Charukamnoetkanok, G. Wollstein, K. A. Townsend, M. L. Gabriele, N. Bahary, X. Y. Wei, J. G. Fujimoto, and J. S. Schuman, "Repeated, Noninvasive, High Resolution Spectral Domain Optical Coherence Tomography Imaging of Zebrafish Embryos," *Molecular Vision,* vol. 14, pp. 2157-2170, Nov 2008.

[55] S. A. Boppart, G. J. Tearney, B. E. Bouma, J. F. Southern, M. E. Brezinski, and J. G. Fujimoto, "Noninvasive Assessment of the Developing Xenopus Cardiovascular System Using Optical Coherence Tomography," *Proceedings of the National Academy of Sciences of the United States of America,* vol. 94, pp. 4256-4261, April 29, 1997 1997.

[56] M. W. Jenkins, O. Q. Chughtai, A. N. Basavanhally, M. Watanabe, and A. M. Rollins, "In Vivo Gated 4d Imaging of the Embryonic Heart Using Optical

Coherence Tomography," *Journal of Biomedical Optics,* vol. 12, pp. 030505-3, 2007.

[57] M. W. Jenkins, F. Rothenberg, D. Roy, V. P. Nikolski, Z. Hu, M. Watanabe, D. L. Wilson, I. R. Efimov, and A. M. Rollins, "4d Embryonic Cardiography Using Gated Optical Coherence Tomography," *Opt. Express,* vol. 14, pp. 736-748, 2006.

[58] K. V. Larin, I. V. Larina, M. Liebling, and M. E. Dickinson, "Live Imaging of Early Developmental Processes in Mammalian Embryos with Optical Coherence Tomography," *Journal of Innovative Optical Health Sciences,* vol. 2, pp. 253-259, Jan 2009.

[59] I. V. Larina, S. Ivers, S. Syed, M. E. Dickinson, and K. V. Larin, "Hemodynamic Measurements from Individual Blood Cells in Early Mammalian Embryos with Doppler Swept Source Oct," *Opt. Lett.,* vol. 34, pp. 986-988, 2009.

[60] I. V. Larina, M. Liebling, M. E. Dickinson, and K. V. Larin, "Imaging of Cardiovascular Dynamics in Early Mouse Embryos with Swept Source Optical Coherence Tomography," in *Optical Coherence Tomography and Coherence Domain Optical Methods in Biomedicine XIII,* San Jose, CA, USA, 2009, pp. 71680E-7.

[61] I. V. Larina, N. Sudheendran, M. Ghosn, J. Jiang, A. Cable, K. V. Larin, and M. E. Dickinson, "Live Imaging of Blood Flow in Mammalian Embryos Using Doppler Swept-Source Optical Coherence Tomography," *J Biomed Opt,* vol. 13, pp. 060506-3, December 2008 2008.

[62] S. H. Syed, K. V. Larin, M. E. Dickinson, and I. V. Larina, "Optical Coherence Tomography for High-Resolution Imaging of Mouse Development in Utero," *J Biomed Opt,* vol. 16, p. 046004, Apr 2011.

[63] S. Yazdanfar, M. Kulkarni, and J. Izatt, "High Resolution Imaging of in Vivo Cardiac Dynamics Using Color Doppler Optical Coherence Tomography," *Optics Express,* vol. 1, pp. 424-431, Dec 1997.

[64] R. M. Payne, M. C. Johnson, J. W. Grant, and A. W. Strauss, "Toward a Molecular Understanding of Congenital Heart Disease," *Circulation,* vol. 91, pp. 494-504, Jan 15 1995.

[65] M. Kouwenberg, R. S. Severijnen, and L. Kapusta, "Congenital Cardiovascular Defects in Children with Intestinal Malrotation," *Pediatric Surgery International,* vol. 24, pp. 257-63, Mar 2008.

[66] W. Rosamond, K. Flegal, K. Furie, A. Go, K. Greenlund, N. Haase, S. M. Hailpern, M. Ho, V. Howard, B. Kissela, S. Kittner, D. Lloyd-Jones, M. McDermott, J. Meigs, C. Moy, G. Nichol, C. O'Donnell, V. Roger, P. Sorlie, J. Steinberger, T. Thom, M. Wilson, and Y. Hong, "Heart Disease and Stroke Statistics--2008 Update: A Report from the American Heart Association Statistics Committee and Stroke Statistics Subcommittee," *Circulation,* vol. 117, pp. e25-146, Jan 2008.

[67] L. Dexter, "Atrial Septal Defect," *British Heart Journal,* vol. 18, pp. 209-25, Apr 1956.

[68] P. J. Gruber and J. A. Epstein, "Development Gone Awry: Congenital Heart Disease," *Circulation Research,* vol. 94, pp. 273-83, Feb 2004.

[69] J. C. Williams, B. G. Barratt-Boyes, and J. B. Lowe, "Supravalvular Aortic Stenosis," *Circulation,* vol. 24, pp. 1311-8, Dec 1961.

[70] F. Fontan and E. Baudet, "Surgical Repair of Tricuspid Atresia," *Thorax,* vol. 26, pp. 240-8, May 1971.

[71] F. Helmcke, N. C. Nanda, M. C. Hsiung, B. Soto, C. K. Adey, R. G. Goyal, and R. P. Gatewood, Jr., "Color Doppler Assessment of Mitral Regurgitation with Orthogonal Planes," *Circulation,* vol. 75, pp. 175-83, Jan 1987.

[72] T. Dahme, H. A. Katus, and W. Rottbauer, "Fishing for the Genetic Basis of Cardiovascular Disease," *Disease Models & Mechanisms,* vol. 2, pp. 18-22, Feb 2009.

[73] W. Rottbauer, K. Baker, Z. G. Wo, M.-A. P. K. Mohideen, H. F. Cantiello, and M. C. Fishman, "Growth and Function of the Embryonic Heart Depend Upon the Cardiac-Specific L-Type Calcium Channel [Alpha]1 Subunit," *Developmental Cell,* vol. 1, pp. 265-275, Aug 2001.

[74] D. M. Garrity, S. Childs, and M. C. Fishman, "The Heartstrings Mutation in Zebrafish Causes Heart/Fin Tbx5 Deficiency Syndrome," *Development,* vol. 129, pp. 4635-4645, Oct 2002.

[75] H. L. Bartlett, L. Sutherland, S. J. Kolker, C. Welp, U. Tajchman, V. Desmarais, and D. L. Weeks, "Transient Early Embryonic Expression of Nkx2-5 Mutations Linked to Congenital Heart Defects in Human Causes Heart Defects in Xenopus Laevis," *Developmental Dynamics,* vol. 236, pp. 2475-84, Sep 2007.

[76] O. B. Cleaver, K. D. Patterson, and P. A. Krieg, "Overexpression of the Tinman-Related Genes Xnkx-2.5 and Xnkx-2.3 in Xenopus Embryos Results in Myocardial Hyperplasia," *Development*, vol. 122, pp. 3549-56, Nov 1996.

[77] H. L. Bartlett and D. L. Weeks, "Lessons from the Lily Pad: Using Xenopus to Understand Heart Disease," *Drug Discovery Today: Disease Models*, vol. 5, pp. 141-146, Apr 2008.

[78] M. L. Kirby, T. F. Gale, and D. E. Stewart, "Neural Crest Cells Contribute to Normal Aorticopulmonary Septation," *Science*, vol. 220, pp. 1059-61, Jun 1983.

[79] A. Tintu, E. Rouwet, S. Verlohren, J. Brinkmann, S. Ahmad, F. Crispi, M. van Bilsen, P. Carmeliet, A. C. Staff, M. Tjwa, I. Cetin, E. Gratacos, E. Hernandez-Andrade, L. Hofstra, M. Jacobs, W. H. Lamers, I. Morano, E. Safak, A. Ahmed, and F. le Noble, "Hypoxia Induces Dilated Cardiomyopathy in the Chick Embryo: Mechanism, Intervention, and Long-Term Consequences," *Public Library of Science One*, vol. 4, p. e5155, Apr 2009.

[80] V. Garg, A. N. Muth, J. F. Ransom, M. K. Schluterman, R. Barnes, I. N. King, P. D. Grossfeld, and D. Srivastava, "Mutations in Notch1 Cause Aortic Valve Disease," *Nature*, vol. 437, pp. 270-4, Sep 8 2005.

[81] D. U. Frank, L. K. Fotheringham, J. A. Brewer, L. J. Muglia, M. Tristani-Firouzi, M. R. Capecchi, and A. M. Moon, "An Fgf8 Mouse Mutant Phenocopies Human 22q11 Deletion Syndrome," *Development*, vol. 129, pp. 4591-603, Oct 2002.

[82] L. Coultas, K. Chawengsaksophak, and J. Rossant, "Endothelial Cells and Vegf in Vascular Development," *Nature*, vol. 438, pp. 937-45, Dec 2005.

[83] K. Theiler, *The House Mouse - Atlas of Embryonic Development*. New York: Springer-Verlag, 1989.

[84] C. J. Drake and P. A. Fleming, "Vasculogenesis in the Day 6.5 to 9.5 Mouse Embryo," *Blood,* vol. 95, pp. 1671-9, Mar 2000.

[85] J. R. Walls, L. Coultas, J. Rossant, and R. M. Henkelman, "Three-Dimensional Analysis of Vascular Development in the Mouse Embryo," *PLoS One,* vol. 3, p. e2853, 2008.

[86] S. J. Conway, A. Kruzynska-Frejtag, P. L. Kneer, M. Machnicki, and S. V. Koushik, "What Cardiovascular Defect Does My Prenatal Mouse Mutant Have, and Why?," *Genesis,* vol. 35, pp. 1-21, Nov 2003.

[87] S. R. May, N. J. Stewart, W. Chang, and A. S. Peterson, "A Titin Mutation Defines Roles for Circulation in Endothelial Morphogenesis," *Developmental Biology,* vol. 270, pp. 31-46, Jun 2004.

[88] W. B. Chapman, "The Effect of the Heart-Beat Upon the Development of the Vascular System in the Chick," *American Journal of Anatomy,* vol. 23, pp. 175-203, Jan 1918.

[89] W. Burggren, S. Warburton, and M. Slivkoff, "Interruption of Cardiac Output Does Not Affect Short-Term Growth and Metabolic Rate in Day 3 and 4 Chick Embryos," *The Journal of Experimental Biology,* vol. 203, pp. 3831-3838, Dec 2000.

[90] B. Hogers, M. C. DeRuiter, A. C. Gittenberger-de Groot, and R. E. Poelmann, "Unilateral Vitelline Vein Ligation Alters Intracardiac Blood Flow Patterns and

Morphogenesis in the Chick Embryo," *Circulation Research,* vol. 80, pp. 473-481, Apr 1997.

[91] J. R. Hove, R. W. Koster, A. S. Forouhar, G. Acevedo-Bolton, S. E. Fraser, and M. Gharib, "Intracardiac Fluid Forces Are an Essential Epigenetic Factor for Embryonic Cardiogenesis," *Nature,* vol. 421, pp. 172-7, Jan 9 2003.

[92] E. A. V. Jones, M. H. Baron, S. E. Fraser, and M. E. Dickinson, "Measuring Hemodynamic Changes During Mammalian Development," *American Journal of Physiology - Heart and Circulatory Physiology,* vol. 287, pp. H1561-1569, Oct 2004.

[93] O. Sakurada, C. Kennedy, J. Jehle, J. D. Brown, G. L. Carbin, and L. Sokoloff, "Measurement of Local Cerebral Blood Flow with Iodo [14c] Antipyrine," *American Journal of Physiology,* vol. 234, pp. H59-66, Jan 1978.

[94] B. F. Tomandl, N. C. Köstner, M. Schempershofe, W. J. Huk, C. Strauss, L. Anker, and P. Hastreiter, "Ct Angiography of Intracranial Aneurysms: A Focus on Postprocessing1," *Radiographics,* vol. 24, pp. 637-655, May 1, 2004 2004.

[95] M. Romijn, H. A. Gratama van Andel, M. A. van Walderveen, M. E. Sprengers, J. C. van Rijn, W. J. van Rooij, H. W. Venema, C. A. Grimbergen, G. J. den Heeten, and C. B. Majoie, "Diagnostic Accuracy of Ct Angiography with Matched Mask Bone Elimination for Detection of Intracranial Aneurysms: Comparison with Digital Subtraction Angiography and 3d Rotational Angiography," *American Journal of Neuoradiology,* vol. 29, pp. 134-9, Jan 2008.

[96] J. C. Baron, "Positron Tomography in Cerebral Ischemia. A Review," *Neuroradiology,* vol. 27, pp. 509-16, Nov 1985.

[97] F. Calamante, D. L. Thomas, G. S. Pell, J. Wiersma, and R. Turner, "Measuring Cerebral Blood Flow Using Magnetic Resonance Imaging Techniques," *Journal of Cerebral Blood Flow & Metabolism,* vol. 19, pp. 701-735, Feb 1999.

[98] J.-K. Guo, C.-H. Chen, J.-D. Lee, and J.-M. Tsai, "3-D Image Reconstruction of Brain Blood Vessels from Angiograms," *Computers & Mathematics with Applications,* vol. 35, pp. 79-94, 1998.

[99] H. E. Thompson, "Clinical Application of Diagnostic Ultrasound in Obstetrics and Gynecology," *The Journal of the Acoustical Society of America,* vol. 44, pp. 1365-72, Nov 1968.

[100] U. Gembruch, G. Knopfle, R. Bald, and M. Hansmann, "Early Diagnosis of Fetal Congenital Heart Disease by Transvaginal Echocardiography," *Ultrasound in Obstetrics and Gynecology,* vol. 3, pp. 310-7, Sep 1993.

[101] P. van Splunder, T. Stijnen, and J. W. Wladimiroff, "Fetal Atrioventricular Flow-Velocity Waveforms and Their Relation to Arterial and Venous Flow-Velocity Waveforms at 8 to 20 Weeks of Gestation," *Circulation,* vol. 94, pp. 1372-8, Sep 15 1996.

[102] L. D. Allan, D. C. Crawford, S. K. Chita, and M. J. Tynan, "Prenatal Screening for Congenital Heart Disease," *British Medical Journal (Clinical Research Ed),* vol. 292, pp. 1717-9, Jun 1986.

[103] C. K. Phoon, O. Aristizabal, and D. H. Turnbull, "40 Mhz Doppler Characterization of Umbilical and Dorsal Aortic Blood Flow in the Early Mouse Embryo," *Ultrasound in Medicine and Biology,* vol. 26, pp. 1275-83, Oct 2000.

[104] Y. Yeh and H. Z. Cummins, "Localised Fluid Flow Measurements with an He-Ne Laser Spectrometer," *Applied Physics Letters,* vol. 4, pp. 176-178, Apr 1964.

[105] J. D. Briers, G. Richards, and X. W. He, "Capillary Blood Flow Monitoring Using Laser Speckle Contrast Analysis (Lasca)," *Journal of Biomedical Optics,* vol. 4, pp. 164-175, 1999.

[106] X. Wang, Y. Pang, G. Ku, X. Xie, G. Stoica, and L. V. Wang, "Noninvasive Laser-Induced Photoacoustic Tomography for Structural and Functional in Vivo Imaging of the Brain," *Nature Biotechnology,* vol. 21, pp. 803-6, Jul 2003.

[107] C. G. Hoelen, F. F. de Mul, R. Pongers, and A. Dekker, "Three-Dimensional Photoacoustic Imaging of Blood Vessels in Tissue," *Optics Letters,* vol. 23, pp. 648-50, Apr 1998.

[108] R. A. Kruger, D. R. Reinecke, and G. A. Kruger, "Thermoacoustic Computed Tomography--Technical Considerations," *Medical Physics,* vol. 26, pp. 1832-1837, 1999.

[109] V. E. Gusev and A. A. Karabutov, *Laser Optoacoustics*. New York: American Institute of Physics 1993.

[110] M. Minsky, "Memoir on Inventing the Confocal Scanning Microscope," *Scanning,* vol. 10, pp. 128-138, 1988.

[111] J. L. Lucitti, E. A. V. Jones, C. Huang, J. Chen, S. E. Fraser, and M. E. Dickinson, "Vascular Remodeling of the Mouse Yolk Sac Requires Hemodynamic Force," *Development,* vol. 134, pp. 3317-3326, 2007.

[112] S. T. Fraser, A. K. Hadjantonakis, K. E. Sahr, S. Willey, O. G. Kelly, E. A. V. Jones, M. E. Dickinson, and M. H. Baron, "Using a Histone Yellow Fluorescent

Protein Fusion for Tagging and Tracking Endothelial Cells in Es Cells and Mice," *Genesis,* vol. 42, pp. 162-171, Jul 2005.

[113] R. M. Zucker, E. S. Hunter, and J. M. Rogers, "Apoptosis and Morphology in Mouse Embryos by Confocal Laser Scanning Microscopy," *Methods-a Companion to Methods in Enzymology,* vol. 18, pp. 473-480, Aug 1999.

[114] R. M. Zucker, "Whole Insect and Mammalian Embryo Imaging with Confocal Microscopy: Morphology and Apoptosis," *Cytometry A,* vol. 69, pp. 1143-52, Nov 2006.

[115] J. Sharpe, U. Ahlgren, P. Perry, B. Hill, A. Ross, J. Hecksher-Sorensen, R. Baldock, and D. Davidson, "Optical Projection Tomography as a Tool for 3d Microscopy and Gene Expression Studies," *Science,* vol. 296, pp. 541-545, April 19, 2002 2002.

[116] W. Luo, D. L. Marks, T. S. Ralston, and S. A. Boppart, "Three-Dimensional Optical Coherence Tomography of the Embryonic Murine Cardiovascular System," *J. Biomed. Opt.,* vol. 11, p. 021014, Mar-Apr 2006.

[117] S. A. Boppart, G. J. Tearney, B. E. Bouma, J. F. Southern, M. E. Brezinski, and J. G. Fujimoto, "Noninvasive Assessment of the Developing Xenopus Cardiovascular System Using Optical Coherence Tomography," *Proc. Natl. Acad. Sci. U S A.,* vol. 94, p. 4256, Apr 29 1997.

[118] M. Bonesi, S. Matcher, and I. Meglinski, "Doppler Optical Coherence Tomography in Cardiovascular Applications," *Laser Phys.,* vol. 20, p. 1491, 2010.

[119] M. Bonesi, S. Proskurin, and I. Meglinski, "Imaging of Subcutaneous Blood Vessels and Flow Velocity Profiles by Optical Coherence Tomography," *Laser Phys.,* vol. 20, p. 891, 2010.

[120] M. Bonesi, D. Y. Churmakov, L. J. Ritchie, and I. V. Meglinski, "Turbulence Monitoring with Doppler Optical Coherence Tomography," *Laser Phys. Lett.,* vol. 4, p. 304, 2007.

[121] B. Veksler, E. Kobzev, M. Bonesi, and I. Meglinski, "Application of Optical Coherence Tomography for Imaging of Scaffold Structure and Micro-Flows Characterization," *Laser Phys. Lett.,* vol. 5, p. 236, 2008.

[122] M. Alexander, L. F. Rojas-Ochoa, M. Leser, and P. Schurtenberger, "Structure, Dynamics, and Optical Properties of Concentrated Milk Suspensions: An Analogy to Hard-Sphere Liquids," *Journal of Colloid and Interface Science,* vol. 253, pp. 35-46, 2002.

[123] J. A. Raty and K.-E. Peiponen, "Reflectance Study of Milk in the Uv-Visible Range," *Applied Spectroscopy,* vol. 53, pp. 1123-1127, Sep 1999.

[124] G. Mitic, J. Kölzer, J. Otto, E. Plies, G. Sölkner, and W. Zinth, "Time-Gated Transillumination of Biological Tissues and Tissuelike Phantoms," *Applied Optics,* vol. 33, pp. 6699-6710, Oct 1994.

[125] C.-W. Sun, C. C. Yang, Y.-W. Kiang, and C.-W. Lin, "Ultrafast Optics Imaging Based on Polarization Discrimination Techniques in Filamentous Tissues," *Biomedical Engineering: Applications, Basis and Communications,* vol. 14, pp. 237-242, 2002.

[126] N. Sudheendran, "Speckle Variance Oct Imaging of the Vasculature in Live Mammalian Embryos," MSEE, Department of Electrical and Computer Engineering, University of Houston, Houston, 2010.

[127] N. Sudheendran, S. H. Syed, M. E. Dickinson, I. V. Larina, and K. V. Larin, "Speckle Variance Oct Imaging of the Vasculature in Live Mammalian Embryos," *Laser Physics Letters,* vol. 8, pp. 247-252, Mar 2011.

[128] J. Graw, "Eye Development," *Curr Top Dev Biol,* vol. 90, pp. 343-86, 2010.

[129] P. Tucker, L. Laemle, A. Munson, S. Kanekar, E. R. Oliver, N. Brown, H. Schlecht, M. Vetter, and T. Glaser, "The Eyeless Mouse Mutation (Ey1) Removes an Alternative Start Codon from the Rx/Rax Homeobox Gene," *Genesis,* vol. 31, pp. 43-53, Sep 2001.

[130] P. H. Mathers, A. Grinberg, K. A. Mahon, and M. Jamrich, "The Rx Homeobox Gene Is Essential for Vertebrate Eye Development," *Nature,* vol. 387, pp. 603-607, Jun 5 1997.

[131] X. Geng, C. Speirs, O. Lagutin, A. Inbal, W. Liu, L. Solnica-Krezel, Y. Jeong, D. J. Epstein, and G. Oliver, "Haploinsufficiency of Six3 Fails to Activate Sonic Hedgehog Expression in the Ventral Forebrain and Causes Holoprosencephaly," *Dev Cell,* vol. 15, pp. 236-47, Aug 2008.

[132] D. K. Rieger, E. Reichenberger, W. McLean, A. Sidow, and B. R. Olsen, "A Double-Deletion Mutation in the Pitx3 Gene Causes Arrested Lens Development in Aphakia Mice," *Genomics,* vol. 72, pp. 61-72, 02/ 2001.

[133] M. Rosemann, A. Ivashkevich, J. Favor, C. Dalke, S. M. Hölter, L. Becker, I. Rácz, I. Bolle, M. Klempt, B. Rathkolb, S. Kalaydjiev, T. Adler, A. Aguilar, W.

Hans, M. Horsch, J. Rozman, J. Calzada-Wack, S. Kunder, B. Naton, V. Gailus-Durner, H. Fuchs, H. Schulz, J. Beckers, D. H. Busch, J. P. Burbach, M. P. Smidt, L. Quintanilla-Martinez, I. Esposito, T. Klopstock, M. Klingenspor, M. Ollert, E. Wolf, W. Wurst, A. Zimmer, M. H. de Angelis, M. Atkinson, U. Heinzmann, and J. Graw, "Microphthalmia, Parkinsonism, and Enhanced Nociception in Pitx3 (416insg) Mice," *Mammalian genome : official journal of the International Mammalian Genome Society,* vol. 21, pp. 13-27, 02/ 2010.

[134] E. V. Semina, J. C. Murray, R. Reiter, R. F. Hrstka, and J. Graw, "Deletion in the Promoter Region and Altered Expression of Pitx3 Homeobox Gene in Aphakia Mice," *Hum Mol Genet,* vol. 9, pp. 1575-85, Jul 1 2000.

[135] R. S. Smith, A. Zabaleta, T. Kume, O. V. Savinova, S. H. Kidson, J. E. Martin, D. Y. Nishimura, W. L. Alward, B. L. Hogan, and S. W. John, "Haploinsufficiency of the Transcription Factors Foxc1 and Foxc2 Results in Aberrant Ocular Development," *Hum Mol Genet,* vol. 9, pp. 1021-32, Apr 12 2000.

[136] M. Burmeister, J. Novak, M. Y. Liang, S. Basu, L. Ploder, N. L. Hawes, D. Vidgen, F. Hoover, D. Goldman, V. I. Kalnins, T. H. Roderick, B. A. Taylor, M. H. Hankin, and R. R. McInnes, "Ocular Retardation Mouse Caused by Chx10 Homeobox Null Allele: Impaired Retinal Progenitor Proliferation and Bipolar Cell Differentiation," *Nat Genet,* vol. 12, pp. 376-84, Apr 1996.

[137] D. J. Horsford, M. T. T. Nguyen, G. C. Sellar, R. Kothary, H. Arnheiter, and R. R. McInnes, "Chx10 Repression of Mitf Is Required for the Maintenance of Mammalian Neuroretinal Identity," *Development,* vol. 132, pp. 177-187, Jan 2005.

[138] Y. J. Ai, Z. Zheng, A. O'Brien-Jenkins, D. J. Bernard, T. Wynshaw-Boris, C. Ning, R. Reynolds, S. Segal, K. Huang, and D. Stambolian, "A Mouse Model of Galactose-Induced Cataracts," *Human Molecular Genetics,* vol. 9, pp. 1821-1827, Jul 22 2000.

[139] M. G. Anderson, R. S. Smith, N. L. Hawes, A. Zabaleta, B. Chang, J. L. Wiggs, and S. W. M. John, "Mutations in Genes Encoding Melanosomal Proteins Cause Pigmentary Glaucoma in Dba/2j Mice," *Nature Genetics,* vol. 30, pp. 81-85, Jan 2002.

[140] J. J. Windle, D. M. Albert, J. M. Obrien, D. M. Marcus, C. M. Disteche, R. Bernards, and P. L. Mellon, "Retinoblastoma in Transgenic Mice," *Nature,* vol. 343, pp. 665-669, Feb 15 1990.

[141] D. M. Albert, C. L. Wilkerson, J. M. Lokken, and J. J. Windle, "The Role of over Expression of N-Myc in Retinoblastoma Development in Transgenic Mice.," *Investigative Ophthalmology & Visual Science,* vol. 38, pp. 2240-2240, Mar 15 1997.

[142] B. R. Smith, G. A. Johnson, E. V. Groman, and E. Linney, "Magnetic Resonance Microscopy of Mouse Embryos," *Proc Natl Acad Sci U S A,* vol. 91, pp. 3530-3, Apr 26 1994.

[143] M. Dhenain, S. W. Ruffins, and R. E. Jacobs, "Three-Dimensional Digital Mouse Atlas Using High-Resolution Mri," *Developmental Biology,* vol. 232, pp. 458-470, Apr 15 2001.

[144] P. Parasoglou, C. A. Berrios-Otero, B. J. Nieman, and D. H. Turnbull, "High-Resolution Mri of Early-Stage Mouse Embryos," *Nmr in Biomedicine,* vol. 26, pp. 224-231, Feb 2013.

[145] T. V. Tkatchenko, Y. M. Shen, and A. V. Tkatchenko, "Analysis of Postnatal Eye Development in the Mouse with High-Resolution Small Animal Magnetic Resonance Imaging," *Investigative Ophthalmology & Visual Science,* vol. 51, pp. 21-27, Jan 2010.

[146] D. H. Turnbull and S. Mori, "Mri in Mouse Developmental Biology," *NMR Biomed,* vol. 20, pp. 265-74, May 2007.

[147] D. H. Turnbull, T. S. Bloomfield, H. S. Baldwin, F. S. Foster, and A. L. Joyner, "Ultrasound Backscatter Microscope Analysis of Early Mouse Embryonic Brain-Development," *Proceedings of the National Academy of Sciences of the United States of America,* vol. 92, pp. 2239-2243, Mar 14 1995.

[148] S. Srinivasan, H. S. Baldwin, O. Aristizabal, L. Kwee, M. Labow, M. Artman, and D. H. Turnbull, "Noninvasive, in Utero Imaging of Mouse Embryonic Heart Development with 40-Mhz Echocardiography," *Circulation,* vol. 98, pp. 912-8, Sep 1 1998.

[149] S. W. John, R. S. Smith, O. V. Savinova, N. L. Hawes, B. Chang, D. Turnbull, M. Davisson, T. H. Roderick, and J. R. Heckenlively, "Essential Iris Atrophy, Pigment Dispersion, and Glaucoma in Dba/2j Mice," *Invest Ophthalmol Vis Sci,* vol. 39, pp. 951-62, May 1998.

[150] F. S. Foster, M. Zhang, A. S. Duckett, V. Cucevic, and C. J. Pavlin, "In Vivo Imaging of Embryonic Development in the Mouse Eye by Ultrasound Biomicroscopy," *Invest Ophthalmol Vis Sci,* vol. 44, pp. 2361-2366, Jun 2003.

[151] A. S. Brown, L. Leamen, V. Cucevic, and F. S. Foster, "Quantitation of Hemodynamic Function During Developmental Vascular Regression in the Mouse Eye," *Invest Ophthalmol Vis Sci,* vol. 46, pp. 2231-7, Jul 2005.

[152] R. H. Silverman, F. Kong, Y. C. Chen, H. O. Lloyd, H. H. Kim, J. M. Cannata, K. K. Shung, and D. J. Coleman, "High-Resolution Photoacoustic Imaging of Ocular Tissues," *Ultrasound Med Biol,* vol. 36, pp. 733-42, May 2010.

[153] I. V. Larina, S. H. Syed, N. Sudheendran, P. A. Overbeek, M. E. Dickinson, and K. V. Larin, "Optical Coherence Tomography for Live Phenotypic Analysis of Embryonic Ocular Structures in Mouse Models," *Journal of Biomedical Optics,* vol. 17, p. 081410, 2012.

[154] C. Mouse Genome Sequencing, R. H. Waterston, K. Lindblad-Toh, E. Birney, J. Rogers, J. F. Abril, P. Agarwal, R. Agarwala, R. Ainscough, M. Alexandersson, P. An, S. E. Antonarakis, J. Attwood, R. Baertsch, J. Bailey, K. Barlow, S. Beck, E. Berry, B. Birren, T. Bloom, P. Bork, M. Botcherby, N. Bray, M. R. Brent, D. G. Brown, S. D. Brown, C. Bult, J. Burton, J. Butler, R. D. Campbell, P. Carninci, S. Cawley, F. Chiaromonte, A. T. Chinwalla, D. M. Church, M. Clamp, C. Clee, F. S. Collins, L. L. Cook, R. R. Copley, A. Coulson, O. Couronne, J. Cuff, V. Curwen, T. Cutts, M. Daly, R. David, J. Davies, K. D. Delehaunty, J. Deri, E. T. Dermitzakis, C. Dewey, N. J. Dickens, M. Diekhans, S. Dodge, I. Dubchak, D. M. Dunn, S. R. Eddy, L. Elnitski, R. D. Emes, P. Eswara, E. Eyras, A. Felsenfeld, G.

A. Fewell, P. Flicek, K. Foley, W. N. Frankel, L. A. Fulton, R. S. Fulton, T. S. Furey, D. Gage, R. A. Gibbs, G. Glusman, S. Gnerre, N. Goldman, L. Goodstadt, D. Grafham, T. A. Graves, E. D. Green, S. Gregory, R. Guigo, M. Guyer, R. C. Hardison, D. Haussler, Y. Hayashizaki, L. W. Hillier, A. Hinrichs, W. Hlavina, T. Holzer, F. Hsu, A. Hua, T. Hubbard, A. Hunt, I. Jackson, D. B. Jaffe, L. S. Johnson, M. Jones, T. A. Jones, A. Joy, M. Kamal, E. K. Karlsson, D. Karolchik, A. Kasprzyk, J. Kawai, E. Keibler, C. Kells, W. J. Kent, A. Kirby, D. L. Kolbe, I. Korf, R. S. Kucherlapati, E. J. Kulbokas, D. Kulp, T. Landers, J. P. Leger, S. Leonard, I. Letunic, R. Levine, J. Li, M. Li, C. Lloyd, S. Lucas, B. Ma, D. R. Maglott, E. R. Mardis, L. Matthews, E. Mauceli, J. H. Mayer, M. McCarthy, W. R. McCombie, S. McLaren, K. McLay, J. D. McPherson, J. Meldrim, B. Meredith, J. P. Mesirov, W. Miller, T. L. Miner, E. Mongin, K. T. Montgomery, M. Morgan, R. Mott, J. C. Mullikin, D. M. Muzny, W. E. Nash, J. O. Nelson, M. N. Nhan, R. Nicol, Z. Ning, C. Nusbaum, M. J. O'Connor, Y. Okazaki, K. Oliver, E. Overton-Larty, L. Pachter, G. Parra, K. H. Pepin, J. Peterson, P. Pevzner, R. Plumb, C. S. Pohl, A. Poliakov, T. C. Ponce, C. P. Ponting, S. Potter, M. Quail, A. Reymond, B. A. Roe, K. M. Roskin, E. M. Rubin, A. G. Rust, R. Santos, V. Sapojnikov, B. Schultz, J. Schultz, M. S. Schwartz, S. Schwartz, C. Scott, S. Seaman, S. Searle, T. Sharpe, A. Sheridan, R. Shownkeen, S. Sims, J. B. Singer, G. Slater, A. Smit, D. R. Smith, B. Spencer, A. Stabenau, N. Stange-Thomann, C. Sugnet, M. Suyama, G. Tesler, J. Thompson, D. Torrents, E. Trevaskis, J. Tromp, C. Ucla, A. Ureta-Vidal, J. P. Vinson, A. C. Von Niederhausern, C. M. Wade, M. Wall, R. J. Weber, R. B. Weiss, M. C. Wendl, A. P. West, K. Wetterstrand, R.

Wheeler, S. Whelan, J. Wierzbowski, D. Willey, S. Williams, R. K. Wilson, E. Winter, K. C. Worley, D. Wyman, S. Yang, S. P. Yang, E. M. Zdobnov, M. C. Zody and E. S. Lander, "Initial Sequencing and Comparative Analysis of the Mouse Genome," *Nature,* vol. 420, pp. 520-62, Dec 5 2002.

[155] C. Colantuoni, B. K. Lipska, T. Ye, T. M. Hyde, R. Tao, J. T. Leek, E. A. Colantuoni, A. G. Elkahloun, M. M. Herman, D. R. Weinberger, and J. E. Kleinman, "Temporal Dynamics and Genetic Control of Transcription in the Human Prefrontal Cortex," *Nature,* vol. 478, pp. 519-23, Oct 27 2011.

[156] V. B. Mountcastle, "The Columnar Organization of the Neocortex," *Brain,* vol. 120, pp. 701-722, Apr 1997.

[157] P. Rakic, "Neurons in Rhesus-Monkey Visual-Cortex - Systematic Relation between Time of Origin and Eventual Disposition," *Science,* vol. 183, pp. 425-427, 1974.

[158] P. Rakic, "Specification of Cerebral Cortical Areas," *Science,* vol. 241, pp. 170-176, Jul 8 1988.

[159] S. Krauss, T. Johansen, V. Korzh, and A. Fjose, "Expression Pattern of Zebrafish Pax Genes Suggests a Role in Early Brain Regionalization," *Nature,* vol. 353, pp. 267-70, Sep 19 1991.

[160] S. Martinez, "The Isthmic Organizer and Brain Regionalization," *Int J Dev Biol,* vol. 45, pp. 367-71, 2001.

[161] N. Liscovitch and G. Chechik, "Specialization of Gene Expression During Mouse Brain Development," *PLoS Comput Biol,* vol. 9, p. e1003185, Sep 2013.

[162] M. E. MacDonald, C. M. Ambrose, M. P. Duyao, R. H. Myers, C. Lin, L. Srinidhi, G. Barnes, S. A. Taylor, M. James, N. Groot, H. MacFarlane, B. Jenkins, M. A. Anderson, N. S. Wexler, J. F. Gusella, G. P. Bates, S. Baxendale, H. Hummerich, S. Kirby, M. North, S. Youngman, R. Mott, G. Zehetner, Z. Sedlacek, A. Poustka, A.-M. Frischauf, H. Lehrach, A. J. Buckler, D. Church, L. Doucette-Stamm, M. C. O'Donovan, L. Riba-Ramirez, M. Shah, V. P. Stanton, S. A. Strobel, K. M. Draths, J. L. Wales, P. Dervan, D. E. Housman, M. Altherr, R. Shiang, L. Thompson, T. Fielder, J. J. Wasmuth, D. Tagle, J. Valdes, L. Elmer, M. Allard, L. Castilla, M. Swaroop, K. Blanchard, F. S. Collins, R. Snell, T. Holloway, K. Gillespie, N. Datson, D. Shaw, and P. S. Harper, "A Novel Gene Containing a Trinucleotide Repeat That Is Expanded and Unstable on Huntington's Disease Chromosomes," *Cell,* vol. 72, pp. 971-983, 3/26/ 1993.

[163] M. Wu, D. F. Chen, T. Sasaoka, and S. Tonegawa, "Neural Tube Defects and Abnormal Brain Development in F52-Deficient Mice," *Proc Natl Acad Sci U S A,* vol. 93, pp. 2110-5, Mar 5 1996.

[164] S. C. Vernes, P. L. Oliver, E. Spiteri, H. E. Lockstone, R. Puliyadi, J. M. Taylor, J. Ho, C. Mombereau, A. Brewer, E. Lowy, J. Nicod, M. Groszer, D. Baban, N. Sahgal, J. B. Cazier, J. Ragoussis, K. E. Davies, D. H. Geschwind, and S. E. Fisher, "Foxp2 Regulates Gene Networks Implicated in Neurite Outgrowth in the Developing Brain," *PLoS Genet,* vol. 7, p. e1002145, Jul 2011.

[165] S. Tomita, M. Ueno, M. Sakamoto, Y. Kitahama, M. Ueki, N. Maekawa, H. Sakamoto, M. Gassmann, R. Kageyama, N. Ueda, F. J. Gonzalez, and Y. Takahama, "Defective Brain Development in Mice Lacking the Hif-1 Alpha Gene

in Neural Cells," *Molecular and Cellular Biology,* vol. 23, pp. 6739-6749, Oct 2003.

[166] M. S. Lidow, "Prenatal Cocaine Exposure Adversely Affects Development of the Primate Cerebral-Cortex," *Synapse,* vol. 21, pp. 332-341, Dec 1995.

[167] G. D. Stanwood, R. A. Washington, and P. Levitt, "Identification of a Sensitive Period of Prenatal Cocaine Exposure That Alters the Development of the Anterior Cingulate Cortex," *Cerebral Cortex,* vol. 11, pp. 430-440, May 2001.

[168] M. S. Lidow and Z. M. Song, "Effect of Cocaine on Cell Proliferation in the Cerebral Wall of Monkey Fetuses," *Cerebral Cortex,* vol. 11, pp. 545-551, Jun 2001.

[169] J. E. Bruin, H. C. Gerstein, and A. C. Holloway, "Long-Term Consequences of Fetal and Neonatal Nicotine Exposure: A Critical Review," *Toxicological Sciences,* vol. 116, pp. 364-374, Aug 2010.

[170] J. B. Dwyer, S. C. McQuown, and F. M. Leslie, "The Dynamic Effects of Nicotine on the Developing Brain," *Pharmacology & Therapeutics,* vol. 122, pp. 125-139, May 2009.

[171] K. Kurppa, P. C. Holmberg, E. Kuosma, and L. Saxen, "Coffee Consumption During Pregnancy and Selected Congenital-Malformations - a Nationwide Case-Control Study," *American Journal of Public Health,* vol. 73, pp. 1397-1399, 1983.

[172] O. Algan and P. Rakic, "Radiation-Induced, Lamina-Specific Deletion of Neurons in the Primate Visual Cortex," *Journal of Comparative Neurology,* vol. 381, pp. 335-352, May 12 1997.

[173] E. S. B. C. Ang, V. Gluncic, A. Duque, M. E. Schafer, and P. Rakic, "Prenatal Exposure to Ultrasound Waves Impacts Neuronal Migration in Mice," *Proceedings of the National Academy of Sciences of the United States of America,* vol. 103, pp. 12903-12910, Aug 22 2006.

[174] P. A. May, J. P. Gossage, W. O. Kalberg, L. K. Robinson, D. Buckley, M. Manning, and H. E. Hoyme, "Prevalence and Epidemiologic Characteristics of Fasd from Various Research Methods with an Emphasis on Recent in-School Studies," *Developmental disabilities research reviews,* vol. 15, pp. 176-92, 2009.

[175] C. Camarillo and R. C. Miranda, "Ethanol Exposure During Neurogenesis Induces Persistent Effects on Neural Maturation: Evidence from an Ex Vivo Model of Fetal Cerebral Cortical Neuroepithelial Progenitor Maturation," *Gene Expression,* vol. 14, pp. 159-171, 2008.

[176] S. M. Smith, "Alcohol-Induced Cell Death in the Embryo," *Alcohol Health & Research World,* vol. 21, pp. 287-295, 1997.

[177] C. Creeley, K. Dikranian, S. Johnson, N. Farber, and J. Olney, "Alcohol-Induced Apoptosis of Oligodendrocytes in the Fetal Macaque Brain," *Acta Neuropathologica Communications,* vol. 1, pp. 1-11, 2013/06/12 2013.

[178] S. E. Parnell, D. B. Dehart, T. A. Wills, S. Chen, C. W. Hodge, J. Besheer, H. G. Waage-Baudet, M. E. Charness, and K. K. Sulik, "Maternal Oral Intake Mouse Model for Fetal Alcohol Spectrum Disorders: Ocular Defects as a Measure of Effect," *Alcoholism-Clinical and Experimental Research,* vol. 30, pp. 1791-1798, Oct 2006.

[179] S. Bake, J. D. Tingling, and R. C. Miranda, "Ethanol Exposure During Pregnancy Persistently Attenuates Cranially Directed Blood Flow in the Developing Fetus: Evidence from Ultrasound Imaging in a Murine Second Trimester Equivalent Model," *Alcoholism-Clinical and Experimental Research,* vol. 36, pp. 748-758, May 2012.

[180] P. Rakic, "Mode of Cell Migration to the Superficial Layers of Fetal Monkey Neocortex," *J Comp Neurol,* vol. 145, pp. 61-83, May 1972.

[181] R. L. Sidman and P. Rakic, "Neuronal Migration, with Special Reference to Developing Human Brain: A Review," *Brain Res,* vol. 62, pp. 1-35, Nov 9 1973.

[182] S. A. Anderson and J. A. Frank, "Mri of Mouse Models of Neurological Disorders," *NMR Biomed,* vol. 20, pp. 200-15, May 2007.

[183] B. J. Nieman, J. Bishop, J. Dazai, N. A. Bock, J. P. Lerch, A. Feintuch, X. J. Chen, J. G. Sled, and R. M. Henkelman, "Mr Technology for Biological Studies in Mice," *NMR Biomed,* vol. 20, pp. 291-303, May 2007.

[184] F. C. Norris, J. Betts-Henderson, J. A. Wells, J. O. Cleary, B. M. Siow, S. Walker-Samuel, K. McCue, P. Salomoni, P. J. Scambler, and M. F. Lythgoe, "Enhanced Tissue Differentiation in the Developing Mouse Brain Using Magnetic Resonance Micro-Histology," *Magnetic Resonance in Medicine,* pp. n/a-n/a, 2012.

[185] S. Mori, R. Itoh, J. Zhang, W. E. Kaufmann, P. C. van Zijl, M. Solaiyappan, and P. Yarowsky, "Diffusion Tensor Imaging of the Developing Mouse Brain," *Magn Reson Med,* vol. 46, pp. 18-23, Jul 2001.

[186] J. Zhang, M. I. Miller, C. Plachez, L. J. Richards, P. Yarowsky, P. van Zijl, and S. Mori, "Mapping Postnatal Mouse Brain Development with Diffusion Tensor Microimaging," *Neuroimage,* vol. 26, pp. 1042-51, Jul 15 2005.

[187] Y. Z. Wadghiri, J. A. Blind, X. Duan, C. Moreno, X. Yu, A. L. Joyner, and D. H. Turnbull, "Manganese-Enhanced Magnetic Resonance Imaging (Memri) of Mouse Brain Development," *NMR Biomed,* vol. 17, pp. 613-9, Dec 2004.

[188] M. Wideroe, C. Brekken, A. Kavelaars, T. B. Pedersen, P. E. Goa, C. Heijnen, J. Skranes, and A. M. Brubakk, "Longitudinal Manganese-Enhanced Magnetic Resonance Imaging of Delayed Brain Damage after Hypoxic-Ischemic Injury in the Neonatal Rat," *Neonatology,* vol. 100, pp. 363-72, 2011.

[189] A. E. Deans, Y. Z. Wadghiri, C. A. Berrios-Otero, and D. H. Turnbull, "Mn Enhancement and Respiratory Gating for in Utero Mri of the Embryonic Mouse Central Nervous System," *Magn Reson Med,* vol. 59, pp. 1320-8, Jun 2008.

[190] D. H. Turnbull and F. S. Foster, "In Vivo Ultrasound Biomicroscopy in Developmental Biology," *Trends in Biotechnology,* vol. 20, pp. S29-S33, Aug 2002.

[191] M. Olsson, K. Campbell, and D. H. Turnbull, "Specification of Mouse Telencephalic and Mid-Hindbrain Progenitors Following Heterotopic Ultrasound-Guided Embryonic Transplantation," *Neuron,* vol. 19, pp. 761-772, Oct 1997.

[192] A. M. Liu, A. L. Joyner, and D. H. Turnbull, "Alteration of Limb and Brain Patterning in Early Mouse Embryos by Ultrasound-Guided Injection of Shh-Expressing Cells," *Mechanisms of Development,* vol. 75, pp. 107-115, Jul 1998.

[193] P. U. Devi, R. Suresh, and M. P. Hande, "Effect of Fetal Exposure to Ultrasound on the Behavior of the Adult-Mouse," *Radiation Research,* vol. 141, pp. 314-317, Mar 1995.

[194] I. Bystron, C. Blakemore, and P. Rakic, "Development of the Human Cerebral Cortex: Boulder Committee Revisited," *Nat Rev Neurosci,* vol. 9, pp. 110-22, Feb 2008.

[195] N. Sudheendran, S. Bake, R. C. Miranda, and K. V. Larin, "Comparative Assessments of the Effects of Alcohol Exposure on Fetal Brain Development Using Optical Coherence Tomography and Ultrasound Imaging," *Journal of Biomedical Optics,* vol. 18, Feb 2013.

[196] H. G. Blaas and S. H. Eik-Nes, "Sonoembryology and Early Prenatal Diagnosis of Neural Anomalies," *Prenat Diagn,* vol. 29, pp. 312-25, Apr 2009.

[197] T. M. Roebuck, S. N. Mattson, and E. P. Riley, "A Review of the Neuroanatomical Findings in Children with Fetal Alcohol Syndrome or Prenatal Exposure to Alcohol," *Alcohol Clin Exp Res,* vol. 22, pp. 339-44, Apr 1998.

[198] S. K. Clarren, E. C. Alvord, Jr., S. M. Sumi, A. P. Streissguth, and D. W. Smith, "Brain Malformations Related to Prenatal Exposure to Ethanol," *J Pediatr,* vol. 92, pp. 64-7, Jan 1978.